Journal of Physics D: Applied Physics

TOPICAL REVIEW

Total-reflection high-energy positron diffraction (TRHEPD) for structure determination of the topmost and immediate sub-surface atomic layers

To cite this article: Yuki Fukaya *et al* 2019 *J. Phys. D: Appl. Phys.* **52** 013002

IOP Publishing Journal of Physics D: Applied Physics

J. Phys. D: Appl. Phys. **52** (2019) 013002 (19pp) https://doi.org/10.1088/1361-6463/aadf14

Topical Review

Total-reflection high-energy positron diffraction (TRHEPD) for structure determination of the topmost and immediate sub-surface atomic layers

Yuki Fukaya[1], Atsuo Kawasuso[2], Ayahiko Ichimiya[3,4] and Toshio Hyodo[4]

[1] Advanced Science Research Center, Japan Atomic Energy Agency, 2-4 Shirakata, Tokai, Naka, Ibaraki 319-1195, Japan
[2] National Institutes for Quantum and Radiological Science and Technology, 1233, Watanuki, Takasaki, Gunma, 370-1292, Japan
[3] Nagoya University, Furo-cho, Chikusa-ku, Nagoya 464-8601, Japan
[4] Institute of Materials Structure Science, High Energy Accelerator Research Organization (KEK), 1-1 Oho, Tsukuba, Ibaraki 305-0801, Japan

E-mail: fukaya.yuki99@jaea.go.jp and hyodot@post.kek.jp

Received 31 May 2018, revised 13 August 2018
Accepted for publication 5 September 2018
Published 25 October 2018

Abstract

Total-reflection high-energy positron diffraction (TRHEPD) has recently been developed to investigate the surface structure (atomic geometry) and surface properties of materials. It is the positron (the antiparticle of the electron) counterpart of reflection high-energy electron diffraction (RHEED). Depending on the glancing angle of incidence, positrons are totally reflected from the surface or shallowly penetrate into the bulk of the sample solid. Thus, it is possible to obtain information about the topmost and immediate sub-surface layers without the background effect of the bulk. In this review, this distinctive feature of the TRHEPD process and some of the results on surface structures and characteristics are described.

Keywords: positron, diffraction, surface, structure, total-reflection

(Some figures may appear in colour only in the online journal)

1. Introduction

The key components of materials research are two-fold: the analysis of the atomic structure of materials, i.e. detailed positions of individual atoms; and that of their characteristics or functions. The same is true for the research of the surfaces. Recent progress in nanotechnology increasingly requires the study of material surfaces. Accompanied by the progress in vacuum technology, various tools for investigating the surface atomic structure and properties have been developed with increasing reliability.

X-ray diffraction (XRD) has long been the standard technique used to elucidate the structure three-dimensionally, such as in the crystals of new materials, complex proteins, etc. For the study of 2D surface structures, surface-sensitivity of the tools is crucial because the volume fraction of the surface to the bulk is extremely small. Various tools have been developed and refined for the analysis of structure, such as scanning tunnelling microscopy (STM), atomic force microscopy (AFM), low-energy electron diffraction (LEED) [1], reflection high-energy electron diffraction (RHEED) [2], and surface XRD (SXRD) [3]. Diffraction of the positron, the

antiparticle of the electron, is also used for this purpose. With advantages such as the absence of exchange interaction, low-energy positron diffraction (LEPD), the positron counterpart of LEED, affords a reliable technique for use in surface structure analysis [4]. Also, LEPD holography [5] and the analysis of LEPD patterns using the surface Patterson function [6] have been proposed as a direct method of surface structure determination. In 1992, TRHEPD (initially called reflection high-energy positron diffraction, RHEPD, in direct analogy with RHEED) was proposed by Ichimiya [7], who pointed out that the total reflection of positrons could be valuable for studying the surface structure and properties of the topmost surface. In 1998, a TRHEPD (still called RHEPD) pattern from a H-terminated Si(1 1 1) surface was first observed by Kawasuso and Okada [8] using apparatus with a radioisotope-based positron beam. This method has since been used for investigations of various surface structures and phase transitions [9]. More recently however, an electron linear accelerator (linac)-based TRHEPD apparatus has been developed [10, 11]. The subsequent improvement in beam quality has made it possible to observe clearer TRHEPD patterns within a much shorter measurement time [12, 13].

The present review reports the characteristic properties of THREPD and some of the recent results by this method. In section 2, the total reflection of positrons at solid surfaces is detailed, with the theory of TRHEPD briefly described in section 3. The apparatus used in TRHEPD studies is described in section 4 and in appendix A. Experimental evidence for the surface sensitivity of the technique is given in section 5. In section 6, examples of the surface structure analysis by TRHEPD are presented. In section 7, some applications of TRHEPD to surface science are reported, followed by a summary section. Preparation of the positron beam for TRHEPD is described in appendix A. Appendix B describes the rocking curve analysis of the TRHEPD patterns primarily used for the surface structure analysis.

The use of the positrons in surface science including the diffraction methods has recently been reviewed by Hugenschmidt [14]

2. Total reflection of positrons

Figure 1 shows the schematic diagram of the TRHEPD process; the experimental set-up is essentially the same as RHEED. The positron beam with a fixed energy of 10–20 keV is incident on the crystal surface at a varying glancing angle, θ, and the pattern of the diffracted beam is recorded. The intensity distributions in a diffraction pattern and a rocking curve, i.e. the glancing angle dependence of the intensity of a particular spot in a diffraction pattern (see appendix B) give information on the detailed atomic geometry of the topmost and sub-surface.

The reasons for the surface sensitivity of TRHEPD are two-fold: one is in common with LEED, RHEED and LEPD; and the other is unique to TRHEPD. With regard to the first point, neither the *low* energy for LEED (50–500 eV) nor the *grazing*

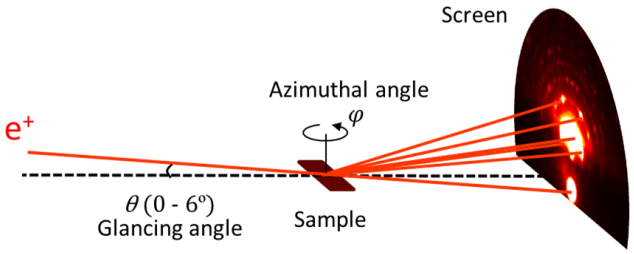

Figure 1. Schematic diagram of total-reflection high-energy positron diffraction (TRHEPD) method. The positron beam (e^+) accelerated to 10–20 keV is incident on the sample surface at a glancing angle (θ) and the diffraction pattern for a fixed azimuthal angle (φ) is observed on the screen.

incident angle for RHEED (10–20 keV and $< 6°$) is the origin of the surface sensitivity. Both the energy and the incident angle are simply chosen to satisfy the Bragg condition

$$2\,d\sin\theta = n\lambda. \tag{1}$$

In back-scattering LEED geometry, $\sin\theta$ is of the order of unity, so that the electron energy should be around 100 eV to give a de-Broglie wavelength, λ, of the same order of magnitude as the lattice constant, d, of the sample. In the forward-scattering RHEED geometry, $\sin\theta$ is smaller by one order of magnitude than that for LEED, so that appropriate wavelength must be smaller by one order of magnitude and hence the electron energy must be around 10 keV, two orders of magnitudes greater. The origin of their surface sensitivity is inelastic scattering. Since inelastic scattering destroys coherence, only the electrons elastically scattered out of the sample without undergoing an inelastic scattering process contribute to the diffraction pattern. The same is true for the positron counterparts, LEPD and TRHEPD.

The second and unique origin of the exceedingly high surface sensitivity of TRHEPD is the universally positive electrostatic potential, V, in every material, resulting from a point-like positive charge of nuclei and extended negative charge of the electron cloud. This comprises a barrier at the surface against the incident positrons. Within non-relativistic approximation, the magnitude of the wave vector, k_0, of the positron beam of kinetic energy, E_0, in vacuum is $\sqrt{2mE_0}/\hbar$, where $\hbar = h/2\pi$, h is the Planck constant and m the electron (positron) mass. When the surface-normal component of the kinetic energy of the positron incident with a glancing angle, θ, is smaller than the value of the average potential energy of the positron inside, eV,

$$E_0\sin^2\theta < eV, \tag{2}$$

then the positron is totally reflected [7]. The critical angle, θ_c, for total reflection is

$$\theta_c = \sin^{-1}\sqrt{eV/E_0}. \tag{3}$$

When θ is gradually increased across θ_c, the positron starts to penetrate into the crystal. The magnitude of the wave vector in the crystal, k, is

$$k = \sqrt{2m\,(E_0 - eV)}/\hbar. \tag{4}$$

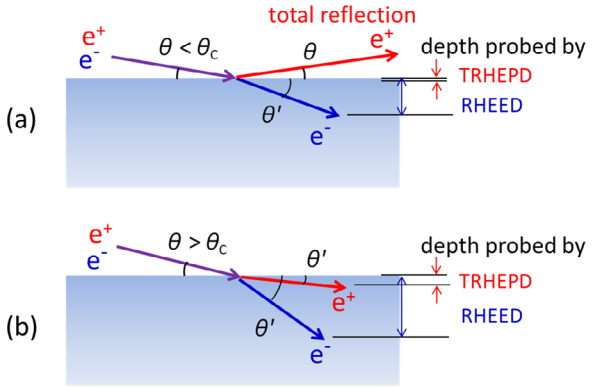

Figure 2. Paths of the positron and electron beams for (a) the glancing angle, θ, smaller than the critical angle of total reflection of the positron, θ_c, and for (b) $\theta > \theta_c$, are schematically shown. Length of the path inside the crystal represents the inelastic mean free path. Possible multiple elastic scatterings are neglected for simplification.

The continuity of the tangential component of the wave vectors on the surface, $k_0 \cos\theta = k \cos\theta'$, leads to the refractive index as

$$n = \frac{\cos\theta}{\cos\theta'} = \frac{k}{k_0} = \sqrt{1 - eV/E_0}, \tag{5}$$

where θ' is the refracted internal glancing angle. Since $k < k_0$, then $\theta' < \theta$, which means that the penetrated positrons are refracted toward the surface. Such refraction makes it possible to continuously change the probing depth from the topmost surface. (Note: we call the whole technique TRHEPD regardless of the desirable inclusion of data from out of the total-reflection condition.)

In contrast, $n > 1$ for electrons, whose average potential energy in the crystal, $-eV$, is negative, and they are refracted away from the surface even when the incident glancing angle is infinitely small. In relation to this, it is well known that lowest-order Bragg reflection spots are not observable in RHEED due to the inevitable increase in the effective glancing angle θ' as well as the decrease in the wavelength. These spots are observable in TRHEPD.

The comparison between the surface sensitivity of RHEED and TRHEPD is schematically summarized in figure 2. The energies of the incident electrons and positrons for these experiments are high enough that the mean-free-paths for the inelastic scattering are essentially the same. Thus, the difference in the direction of the refracted beam results in a difference in the average penetrating depth of the particles before undergoing the first inelastic scattering; the depth probed by positron diffraction is much smaller than that by the electron counterpart. Actually, multiple scattering is significant that dynamical theory (see section 3) is necessary for the analysis.

Figure 3 shows the depth to which 10 keV positrons and electrons in TRHEPD and RHEED, respectively, probe as functions of the incident glancing angle. They are the result of solving the Schrödinger equation using a step-like potential of 12 V and an imaginary potential of 1.2 V representing the inelastic mean free path in Si. The critical angle for total reflection is about 2.0°. For $\theta < \theta_c$, the probing depth is on the order of the size of the atom. Note that the value of

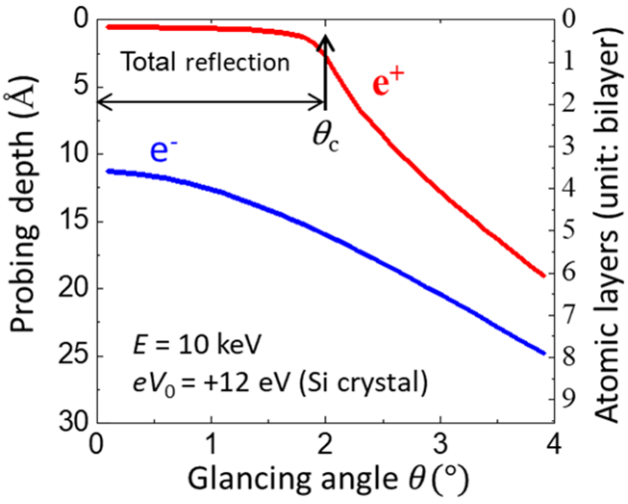

Figure 3. Probing depths of the positron and electron beam with an energy of 10 keV into the surface of a Si crystal as functions of the glancing angle. Red and blue lines indicate the positron and electrons beams, respectively.

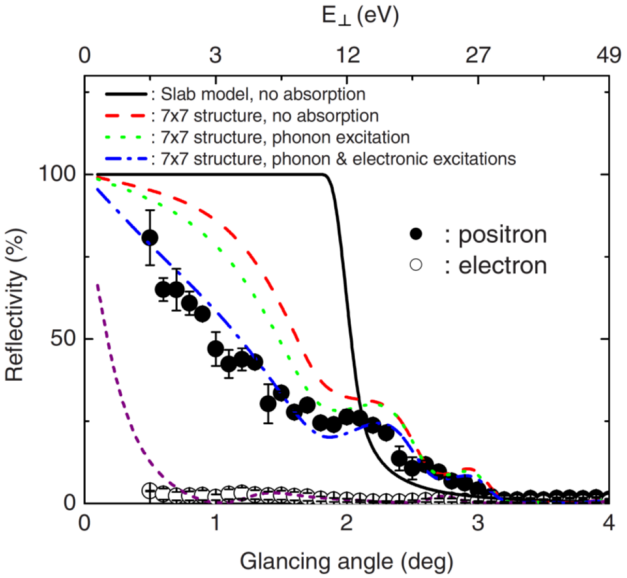

Figure 4. Absolute reflectivity of 0 0 spots for positrons and electrons from a Si(1 1 1)-(7 × 7) surface as functions of the glancing angle under the one-beam condition [16]. The solid line shows the calculated reflectivity without any absorption effects. Reprinted from [16], Copyright 2009 by the American Physical Society.

θ_c for SXRD is considerably smaller (typically 0.2°) and the penetration depth is greater than 20 Å even for $\theta < \theta_c$ [15]. It should be emphasized that TRHEPD is the only diffraction technique developed where the angular region for measurement suitably overlaps with that of the total reflection.

Figure 4 displays absolute reflectivity of 0 0 or the specular spots for positrons and electrons from a Si(1 1 1)-(7 × 7) surface as functions of the glancing angle under the one-beam condition [16]. The solid line shows the reflectivity calculated using a step-like potential without any inelastic scattering. Closed and open circles indicate the measured reflectivity of the positron and electron beams, respectively,

with an energy of 10 keV. The upper horizontal axis denotes the vertical energy, $E_\perp (= E_0 \sin^2\theta)$, of the incident beam. The observed reflectivity for the positron in the total reflection region is considerably below 100%, although it is still much larger than that for the electron. The reasons are (i) a non-flat reconstructed surface structure and (ii) inelastic effects due to surface inelastic scatterings involving phonon and electronic excitations. The calculated results for positrons with the 7×7 structure affecting the ideal total reflection condition, phonon excitations, and electronic excitations, taken into account successively on the basis of the dynamical diffraction theory are shown in figure 4; the purple dashed line shows the result for electrons, including all the interactions.

3. Dynamical diffraction theory

3.1. Basic formalism

The theory of TRHEPD, already used in the calculations shown in figure 4, is briefly introduced in this section. It is the same dynamical theory as that of RHEED, except for the sign of the charge of the incident particle. The theory has been established since the early 1980s [17, 18]. The exchange interaction is not included because it is negligible for electrons of energy around 10 keV or higher. Non-negligible, multiple-scattering effects due to the strong interactions between the electron (positron) and the atoms in the crystal are included. This framework is called the dynamical diffraction theory.

The wave function $\psi(\boldsymbol{r})$ of positrons around a crystal surface is described by the Schrödinger equation

$$-\frac{\hbar^2}{2m}\nabla^2\psi(\boldsymbol{r}) + U(\boldsymbol{r})\psi(\boldsymbol{r}) = E\psi(\boldsymbol{r}), \tag{6}$$

where $U(\boldsymbol{r})$ is the complex potential energy of the positron in the crystal. At and near the surface, the translational periodicity along the surface-normal direction, z, is lost. Periodicity in the directions parallel to the surface remains, but the units of the period are generally larger than those in the bulk due to reconstruction and pertinent relaxation. Thus, the potential energy and the wave function can be expanded in the 2D Fourier series

$$U(\boldsymbol{r}) = \sum_{\boldsymbol{g}} U_{\boldsymbol{g}}(z)\exp(\mathrm{i}\boldsymbol{g}\cdot\boldsymbol{r}_\mathrm{t}), \tag{7}$$

and

$$\psi(\boldsymbol{r}) = \sum_{\boldsymbol{g}} c_{\boldsymbol{g}}(z)\exp[\mathrm{i}(\boldsymbol{k}_{0\mathrm{t}} + \boldsymbol{g})\cdot\boldsymbol{r}_\mathrm{t}], \tag{8}$$

respectively, where $\boldsymbol{g}$ is the 2D reciprocal lattice vector for the (reconstructed) surface, and $\boldsymbol{k}_{0\mathrm{t}}$ and $\boldsymbol{r}_\mathrm{t}$ are the surface-parallel components of $\boldsymbol{k}_0$ and $\boldsymbol{r}$, respectively. By substituting (7) and (8) into (6), the fundamental equation for TRHEPD is obtained,

$$\frac{d^2}{dz^2}c_{\boldsymbol{g}}(z) + \Gamma_{\boldsymbol{g}}^2 c_{\boldsymbol{g}}(z) + \frac{2m}{\hbar^2}\sum_{\boldsymbol{h}} U_{\boldsymbol{g}-\boldsymbol{h}}(z)\, c_{\boldsymbol{h}}(z) = 0, \tag{9}$$

where $\Gamma_{\boldsymbol{g}}^2 = k_0^2 - (\boldsymbol{k}_{0\mathrm{t}} + \boldsymbol{g})^2$. The boundary conditions at the entrance surface (z_s) and the bottom or exit surface (z_b) are, respectively, defined in the forms

$$c_{\boldsymbol{g}}(z_\mathrm{s}) = \delta_{\boldsymbol{g}0}\exp(\mathrm{i}\Gamma_{\boldsymbol{g}} z_\mathrm{s}) + R_{\boldsymbol{g}}\exp(-\mathrm{i}\Gamma_{\boldsymbol{g}} z_\mathrm{s}) \tag{10}$$

and

$$c_{\boldsymbol{g}}(z_\mathrm{b}) = T_{\boldsymbol{g}}\exp(i\Gamma_{\boldsymbol{g}} z_\mathrm{b}), \tag{11}$$

where $R_{\boldsymbol{g}}$ and $T_{\boldsymbol{g}}$ are the amplitudes of reflected and transmitted waves for the $\boldsymbol{g}$th rod, respectively, and $\delta_{\boldsymbol{g}0}$ is Kronecker's delta. To solve (9) with the conditions of (10) and (11), numerical algorithms such as the integration and the multi-slice methods have been developed. Details of the algorithms are given in [2]. The TRHEPD intensity for the $\boldsymbol{g}$th rod is given by $I_{\boldsymbol{g}} = |R_{\boldsymbol{g}}|^2$.

3.2. Crystal potential

The complex potential energy, including that for the inelastic scatterings, is expressed as

$$U = U^{\mathrm{elastic}} + \mathrm{i}\left(U^{\mathrm{TDS}} + U^{\mathrm{el}} + U^{\mathrm{pl}}\right). \tag{12}$$

Here, the real part U^{elastic} is the electrostatic potential energy responsible for the elastic scattering, and the imaginary parts, U^{TDS}, U^{el} and U^{pl} are responsible for the inelastic scatterings due to the thermal diffuse scattering by phonons, electronic excitations and plasmon excitations, respectively. These are highly relevant to the surface sensitivity of RHEED and TRHEPD, as mentioned in section 1.

The Fourier component of U^{elastic} is given by [19]

$$U_{\boldsymbol{g}}^{\mathrm{elastic}} = -\frac{\hbar^2}{2m}\frac{4\pi}{\Omega_0}\sum_{j(\mathrm{unit\ cell})}\exp(-\mathrm{i}\boldsymbol{g}\cdot\boldsymbol{R}_j)\, f(s)\exp\left(-Bs^2\right), \tag{13}$$

where Ω_0 and $\boldsymbol{R}_i$ are the unit cell volume and the position of the ith atom, respectively, and $\boldsymbol{s} = \boldsymbol{g}/4\pi$. $f(s)$ is the elastic atomic scattering factor which may be expressed as a sum of Gaussians, $f(s) = \sum_n a_n \exp\left(-b_n s^2\right)$. The parameters a_n and b_n are listed in the literature [20, 21]. The parameter B is the temperature factor relating to the mean square amplitude, $\langle u^2\rangle$, of the thermal vibrations and is written in the following form within the Einstein approximation [22, 23][5]

$$B = 8\pi^2\langle u^2\rangle = \frac{8\sqrt{3}\pi\hbar^2}{k_\mathrm{B}M_\mathrm{a}\Theta}\left[\frac{1}{2} + \frac{1}{\exp\left(\Theta/\sqrt{3}T\right)-1}\right], \tag{14}$$

where T is the sample temperature and Θ is the Debye temperature, with k_B and M_a the Boltzmann constant and the atomic mass, respectively. Positiveness of $U_{\boldsymbol{g}}^{\mathrm{elastic}}$ is responsible for the total reflection of the positron, which automatically takes place in solving (6) or (9) across the crystal surface.

The Fourier coefficient of the imaginary potential, U^{TDS}, is estimated as [2]

$$U_{\boldsymbol{g}}^{\mathrm{TDS}} = \frac{4.74BZ^2}{\Omega_0\sqrt{E}}\ln\left(\frac{15.4}{BZ^{\frac{2}{3}}} + 1\right)\exp\left(-\frac{Bg^2}{8\pi^2}\right)G_{\boldsymbol{g}} \tag{15}$$

where $G_{\boldsymbol{g}}$ is given as

$$G_{\boldsymbol{g}} = \sum_{j(\mathrm{unit\ cell})}\exp(-\mathrm{i}\boldsymbol{g}\cdot\boldsymbol{R}_j) \tag{16}$$

[5] [23], equation (2.41). This equation is the high temperature limit of equation (14) in the present article.

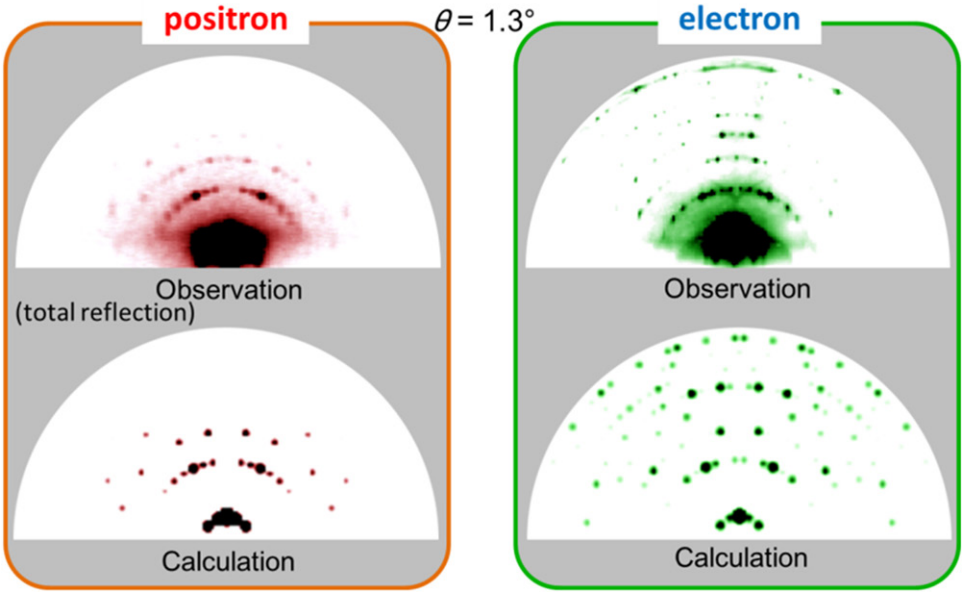

Figure 5. Measured (top) and calculated (bottom) TRHEPD (left) and RHEED (right) patterns from a Si(1 1 1)-(7 × 7) surface for the glancing angle $\theta = 1.3°$ [12]. The energy of the incident positron and electron was 10 keV. The incident azimuths were set along the [1 1 $\bar{2}$] direction. Reprinted from [12]. © 2014 The Japan Society of Applied Physics. All rights reserved.

and E is incident positron energy in eV, and Ω_0 is the unit cell volume in Å^3.

The Fourier coefficient of U^{el} is estimated as [2]

$$U_{\boldsymbol{g}}^{\mathrm{el}} = \frac{s_{\mathrm{A}}^2}{s_{\mathrm{A}}^2+g^2}\frac{147Z^{\frac{1}{3}}}{\Omega_0\sqrt{E}}\left(\ln\left(\frac{8.82\sqrt{E}Z^{\frac{1}{3}}}{\Delta E^{\mathrm{el}}}\right)-\frac{1}{4}\right)G_{\boldsymbol{g}} \qquad (17)$$

where ΔE^{el} is a loss energy of positron by a core electron excitation, S_{A} is the order of magnitude of the first reciprocal lattice.

The Fourier coefficient of U^{pl} is estimated as [2]

$$U_{\boldsymbol{g}}^{\mathrm{pl}} = \frac{1.96\Delta E^{\mathrm{pl}}}{\sqrt{E}}\ln\left(\frac{\lambda_{\mathrm{F}}\sqrt{E}}{12.24}\right)\delta_{0\boldsymbol{g}}\frac{G_{\boldsymbol{g}}}{N_{\mathrm{cell}}} \qquad (18)$$

where ΔE^{pl} is the plasmon loss energy, λ_{F} is the wavelength (in Å) of the electron at the Fermi surface and N_{cell} is the number of atoms in the unit cell.

In the case of compound crystals and alloys including different atoms these potentials could be approximated by summing the contributions from each atom.

4. Experimental apparatus

There are two ways of preparing a source for an energy-tuned positron beam. One way uses a positron-emitting radioisotope such as ^{22}Na, the other employs pair creation from high-energy photons. The photons used for this purpose are those emitted from the bremsstrahlung of accelerated electrons on hitting a heavy metal target, or γ-rays from a nuclear reactor core and those from the n-γ reaction of cadmium. The radioisotope method is handy but beam intensity is limited. The pair creation technique requires a relatively large facility but a higher intensity is achievable.

So far, TRHEPD apparatus have only existed at JAEA and at KEK, both in Japan. The first apparatus was a ^{22}Na-based one made at JAEA by Kawasuso and Okada [8]. In 2010, their experimental chamber was moved to KEK in the quest for a more intense beam created by a dedicated electron linac [10]. Later it was replaced by a newly constructed TRHEPD station [11] with a brightness-enhanced [24–26] positron beam. These systems are described in appendix A.

5. Surface sensitivity of TRHEPD

5.1. Comparison of TRHEPD and RHEED patterns

Figure 5 displays observed and calculated TRHEPD and RHEED patterns of a Si(1 1 1)-(7 × 7) surface at a glancing angle $\theta = 1.3°$ [12]. The total reflection condition is satisfied for TRHEPD. The 7 × 7 reconstructed surface has a so-called DAS structure (figure 6) consisting of dimer atoms, adatoms, and a stacking-fault layer, which was finally revealed by transmission electron diffraction (TED) [27] about 30 years after its discovery. It is clearly seen that the observed patterns are quite different from each other. This demonstrates that, even at the same glancing angle, RHEED probes down to deeper layers compared to TRHEPD, as shown in figure 3.

It is interesting to further notice that the agreement between the observed and calculated RHEED patterns are not as good as those between the corresponding TRHEPD patterns. The dynamical intensity calculations were performed for the atomic configurations determined by the first-principles calculations [28] down to the 3rd atomic layer indicated in figure 6 and the unrelaxed bulk structure for the lower layers. Possible reasons for this discrepancy are that some unknown relaxation may exist below the 3rd layer where RHEED probes and that a higher order calculation with a larger number of diffracted beams (Fourier components) is necessary to reproduce the RHEED pattern. In order to see scatterings from how many atomic layers contribute to the TRHEPD and RHEED patterns, dynamical intensity calculations were performed

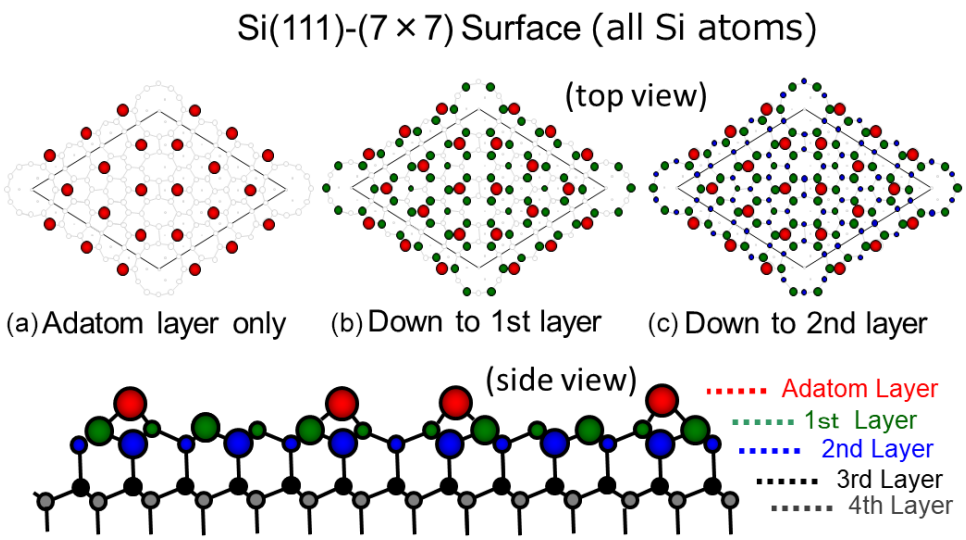

Figure 6. Schematic diagram of the DAS structure of Si(111)-(7 × 7) surface. Red, green, blue, black and grey circles indicate adatoms, first, second, third and fourth layer atoms, respectively, all Si. Reproduced from [12]. © 2014 The Japan Society of Applied Physics. All rights reserved.

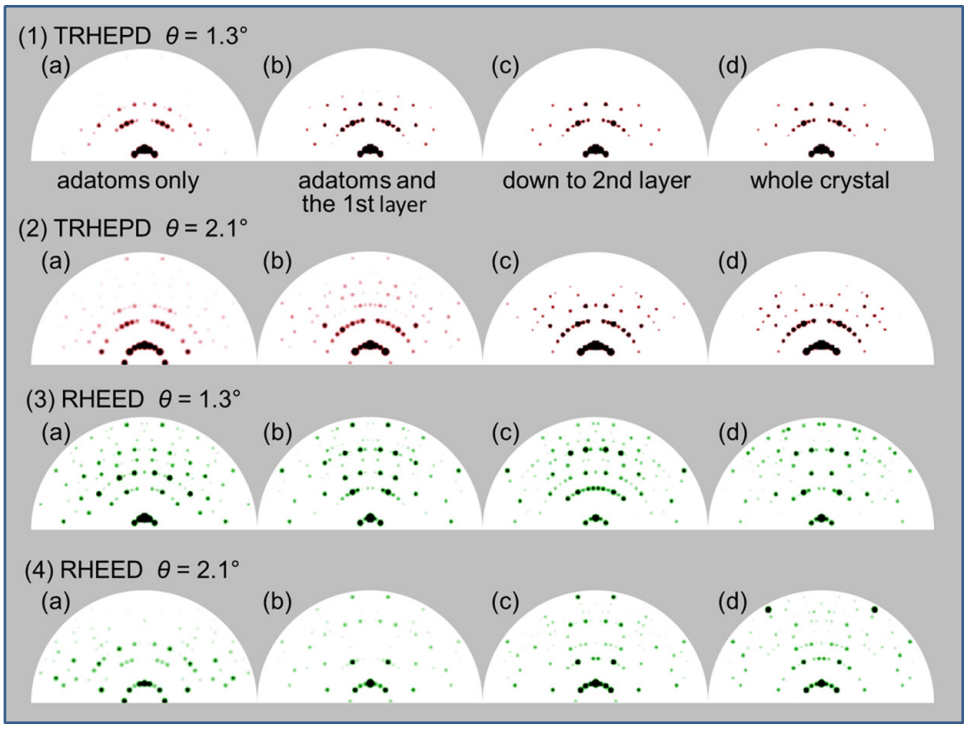

Figure 7. Calculated TRHEPD ((1): $\theta = 1.3°$ and (2): $\theta = 2.1°$) and RHEED ((3): $\theta = 1.3°$ and (4): $\theta = 2.1°$) patterns from the Si(111)-(7 × 7) surface [12]. The incident conditions were the same as those in figure 6. The patterns in (a)–(c) are from the sheets of adatoms only, adatoms and the first layer, and the atoms down to the second-surface layer, respectively. In (d), all the atoms in the whole crystal were included in the calculations. Reproduced from [12]. © 2014 The Japan Society of Applied Physics. All rights reserved.

for the increasing numbers of sheets in the DAS structure using the same code. Figure 7(1-a) shows the calculated TRHEPD patterns for the sheet of the adatoms (figure 6(a)) only, with $\theta = 1.3°(< \theta_c)$. The pattern already reproduces the TRHEPD pattern in figure 7(1-d), which is the same as that in figure 5. The calculation for the sheet consisting of the adatoms and the first layer atoms, as shown in figure 7(1-b), agrees better with figure 7(1-d). This is because some of the first layer atoms are exposed to the vacuum between the rather sparse adatoms. Inclusion of the second layer, figure 7(1-c), does not improve the good agreement any further. Thus, the totally reflected positron beam probes only the atoms exposed to vacuum. Figure 7(2) shows a similar series of the calculated TRHEPD patterns with $\theta = 2.1°(> \theta_c)$. The calculation

with the atoms down to the second layer, figure 7(2-c), is nearly the same as that with the whole crystal, figure 7(2-d). Thus, the positron beam incident at $\theta = 2.1°$ probes down to the second-surface layer but not much more. Figures 7(3) and 7(4) show similar calculations carried out for RHEED patterns. These results indicate that even at $\theta = 1.3°$, the electron beam probes the layers deeper than the second layer.

6. Surface structure analysis with TRHEPD

The TRHEPD method has been used in various surface structure studies. In this section a few typical examples of the results with rocking curve analysis are given. In a measurement, TRHEPD pattern is recorded up to the glancing angle of about 6° in steps of 0.1°, from which the spot intensity is extracted. The intensity of the specular reflection is so high that it takes only about 2 min to take data necessary for each glancing angle with the apparatus at KEK, and thus the measurement for one rocking curve is completed in about 2 h. More details of the rocking curve analysis are given in appendix B.

6.1. Structure of Pt/Ge atomic nanowire

Self-assembled nanowires of metallic atoms formed on semiconductor surfaces have attracted great attention in the pursuit of understanding 1D properties such as the non-Fermi liquid and the Peierls-type metal-insulator transitions. Defect-less nanowires of a periodicity p(4 × 2), as shown in figure 8(a), are formed on Ge(0 0 1) surface by depositing a sub-monolayer of Pt atoms at room temperature [29]. The surface periodicity changes to p(4 × 4) below 80 K [30].

The three major models among many proposed for the structure are shown in figure 8(b): Pt dimer (PD) model [29], tetramer-dimer-chain (TDC) model [31, 32] and the nanowire (NW) model with a Pt coverage of 0.75 monolayers (ML) [33, 34]. Another NW model with a coverage of 0.8125 ML [34] was also proposed for the p(4 × 4) symmetry. Note that the amount of deposited Pt atoms in the sample preparation process is not a conclusive indicator of the structure because some of the deposited atoms evaporate and others penetrate below the surface.

The circles in figure 8(c) shows the TRHEPD rocking curve of the 0 0 (specular) spot measured at 35 K under a one-beam condition (see appendix B) [35]. The lines are the rocking curves calculated for the three models mentioned above, after adjustment of the atomic positions so as to minimize the reliability factor, R (see appendix B). Other proposed structural models with the Pt coverage ranging from 0.25 to 1 ML in [31, 34, 36] were also examined.

Among all the models examined, the NW models with a Pt coverage of 0.75 ML and 0.8125 ML (not shown in figure 8) give the best reliability factor ($R = 1.2\%$). Analysis of the rocking curve in many-beam condition revealed that the former with a modification into a p(4 × 4) symmetry is in better agreement with the experimental data ($R = 1.8\%$) than the latter (2.8%). In the p(4 × 4) symmetry, the adjacent Ge dimers are alternately buckled in the direction normal to the surface.

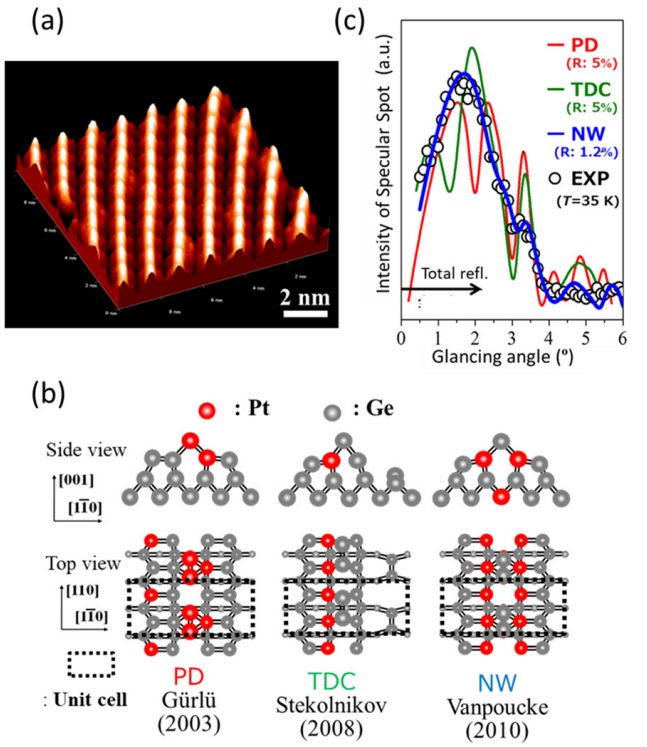

Figure 8. (a) STM image of Ge(0 0 1) p(4 × 2) Pt structure. (b) Schematic drawings of three proposed models: platinum dimer (PD) [29], tetramer dimer chain (TDC) [31, 32] and nanowire (NW) [33, 34] models. The dotted rectangles represent the p(4 × 2) unit cells. (c) TRHEPD rocking curves under the one-beam condition at 35 K [35]. The open circles denote experimental data. The red, green and blue lines are the calculated curves for the PD, TDC and NW models, respectively. Reprinted from [35], Copyright 2012 by the American Physical Society.

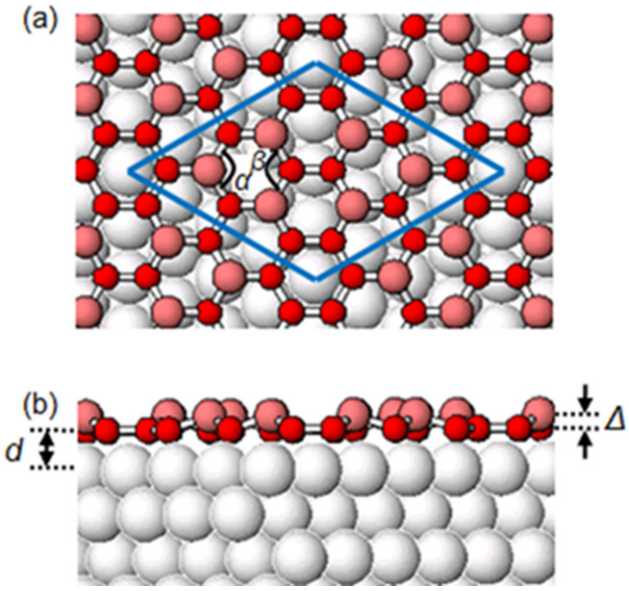

Figure 9. Schematic drawings of silicene on a Ag(1 1 1) surface [43]. Large light red and small dark red circles indicate the upper and lower Si atoms, respectively. Grey circles indicate the Ag atoms. The spacing between the upper and lower Si atoms and the distance between the lower Si atoms and first Ag atoms are denoted by Δ and d, respectively. Reprinted from [43], Copyright 2013 by the American Physical Society.

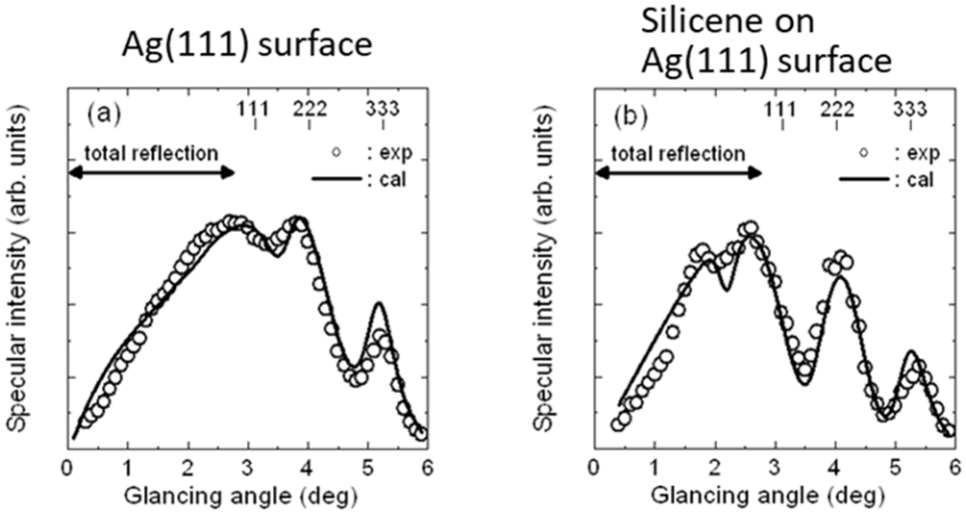

Figure 10. TRHEPD rocking curve for (a) the Ag(1 1 1) and (b) the silicene on a Ag(1 1 1) surface under the one-beam condition at room temperature [43]. Open circles indicate the experimental curve. Solid line shows the calculated curve using the optimum structure parameters. Reprinted from [43], Copyright 2013 by the American Physical Society.

The TRHEPD rocking curve for the 0 0 spot measured in the one-beam condition at room temperature shows a small but distinct difference from the curve at 30 K. It agrees with a structure which has no buckling of the Ge dimers and thus in the p(4 × 2) symmetry.

6.2. Structure determination of two-dimensional (2D) materials on a substrate

Since the isolation and production on a substrate of graphene [37], two-dimensional (2D) materials composed of the group IV elements, graphene (C), silicene (Si), germanene (Ge) and stanene (Sn), have attracted increasing attention as new functional materials for future electronic devices because of the possibility of intriguing properties such as the Dirac cone of the energy band [38]. It is reported that characteristics, such as the electron band structure, vary via interactions with the substrate. Experimental determination of the detailed positions of the atoms in a 2D material, i.e. the buckling, if any, and the distance between the material and the substrate are crucially important to elucidate the characteristics. TRHEPD is most suited for determining these structures.

6.2.1. Silicene on a Ag(1 1 1) surface. Theoretical calculations demonstrated that the shape of the Dirac cone depends on the buckling and the spacing between the silicene and the underlying substrate [39, 40]. The structure of silicene synthesized on a Ag(1 1 1) [41, 42] (shown schematically in figure 9) was analysed by TRHEPD and the buckling predicted by theoretical calculations due to the strong sp^3-bonding character was experimentally verified [43]. TRHEPD rocking curves for the Ag(1 1 1) surface and the silicene on the surface were measured in a one-beam condition, where the incident azimuth was 13° off the $[1\,1\,\bar{2}]$ direction, and the intensities of the 0 0 spot were extracted as a function of the incident glancing angle. The open circles in figure 10 show the results. The surface sensitivity of the method is clearly seen by noticing the

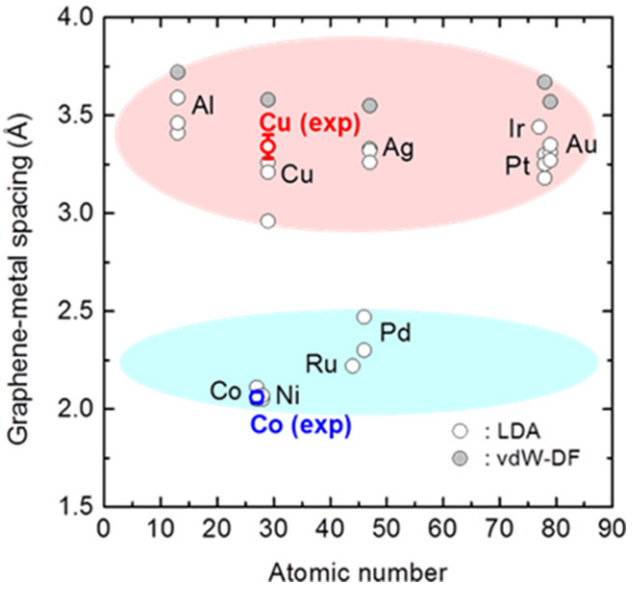

Figure 11. Calculated graphene-substrate distances [45, 47, 50, 51] and the result of TRHEPD measurements [49].

significant difference between the data for (a) Ag(1 1 1) and (b) silicene on Ag(1 1 1).

To determine the atomic positions of the silicene perpendicular to the surface, the rocking curve was calculated with the magnitude of the buckling (Δ) in the silicene and the spacing (d) between the silicene and the Ag substrate varied as free parameters. The best values were determined by minimizing the R factor.

The solid line in figure 10 represents the optimized calculated curve. The optimized values are $\Delta = 0.83$ Å and $d = 2.14$ Å. These values are consistent with the theoretical calculations within uncertainties of ±0.05 Å [41, 42].

To determine the in-plane structure parameters, the 0 0 spot rocking curve was measured along the $[1\,1\,\bar{2}]$ direction. The bond angles α and β were the fitting parameters. The optimum

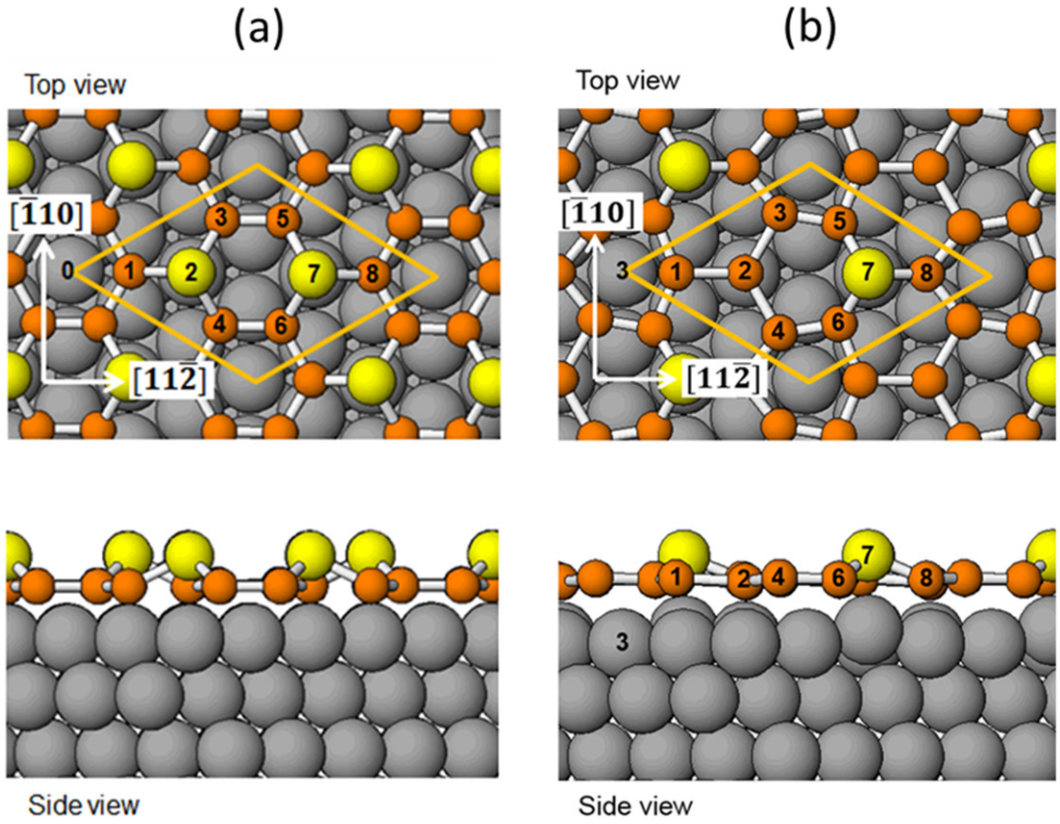

Figure 12. Structure of germanene on an Al(1 1 1) surface; (a) theoretically proposed [55, 58, 59] and (b) determined by TRHEPD [60]. Reproduced from [60]. © IOP Publishing Ltd. All rights reserved.

values of α and β were $\alpha = 112°$ and $\beta = 119°$. These values were in good agreement with the theoretical predictions [41].

6.2.2. Graphene on a Cu(1 1 1) and a Co(0 0 0 1) surface. Graphene has been attracting increasing attention since the report of its isolation, with focus on its features such as high carrier mobility, high thermal conductivity and robust mechanical property [37] and a large spin diffusion length [44]. Theoretical calculations show that the spacing between the graphene and the substrate is classified into two groups, depending on the interaction between them: weak interaction with simple and noble metal substrates; and strong interaction with transition metal substrates [45, 46]. The interaction also modulates the energy dispersion of the so-called Dirac cone for a freestanding graphene [45]. It has been pointed out [47] that the *d*-states of the Co(0 0 0 1) substrate become hybridized with the p_z-states of the graphene, leading to the formation of chemical bonds between them. Furthermore, possible significance of the influence of a long-range van der Waals interaction is suggested [48].

TRHEPD measurements have been performed to experimentally determine the spacing between graphene and metal substrates of Cu(1 1 1) and Co(0 0 0 1) [49]. The theoretically reported graphene-substrate distance and the results of the TRHEPD measurements are summarized in figure 11. The spacing for Cu(1 1 1) was 3.34 ± 0.06 Å, very close to the interlayer spacing in graphite (3.35 Å). That for Co(0 0 0 1) was smaller at 2.06 ± 0.04 Å. No buckling was observed in both cases with the analysis allowing for possible buckling. As for the relaxation of the substrate surface, the position of the surface atoms of Cu(1 1 1) was not changed while that for Co(0 0 0 1) shifted downwards by 0.15 ± 0.02 Å. These results are consistent with the theoretical predictions.

6.2.3. Germanene on an Al(1 1 1) surface. Production of germanene was first reported in 2014 [52–54], and study of this single atomic sheet material on various substrates is rapidly increasing [55–57]. First-principles calculations for germanene on an Al(1 1 1) surface proposed that it has a buckling consisting of the upward shift of two Ge atoms in the 3×3 unit cell from the basic honeycomb structure as shown in figure 12(a), and that the magnitude of the buckling is 1.21–1.23 Å [55, 58, 59]. However, its detailed atomic configuration was not confirmed experimentally by these studies.

Fukaya *et al* [60] investigated the atomic configuration of germanene on an Al(1 1 1) surface. Rocking curves of several spots were measured, with the incident beam directions along the [1 1 $\bar{2}$] and [1 $\bar{1}$ 0]. It was found that the measured intensities of the $-1/3$ 1/3, $-2/3$ 2/3, and -1 1 spots for the incidence along the [$\bar{1}$ 1 0] direction, are significantly different from those for the 1/3 $-1/3$, 2/3 $-2/3$, and 1 -1 spots, respectively. This results in the corresponding difference in their glancing angle dependence or the shapes of the rocking curves, as shown by the open circles in figure 13. This excludes the possibility of the proposed symmetrical buckling of two Ge atoms in the unit cell of the germanene layer. In contrast, the results for the incidence along the [1 1 $\bar{2}$] direction showed that the rocking curves for the $-1/3$ $-1/3$,

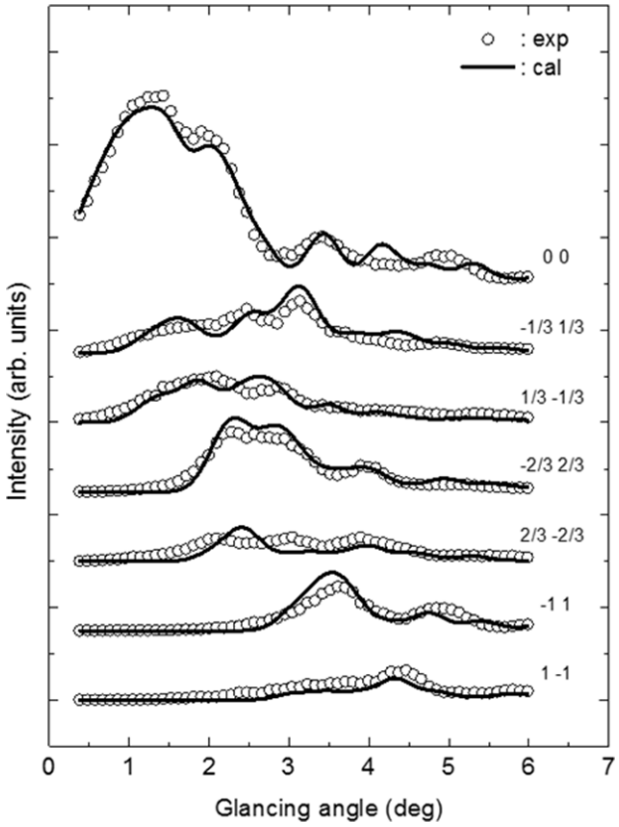

Figure 13. TRHEPD rocking curves for germanene on an Al(1 1 1) substrate along the [1 $\bar{1}$ 0] direction [60]. Open circles and solid lines indicate the measured intensities and the curves calculated using the optimized parameters, respectively. Reproduced from [60]. © IOP Publishing Ltd. All rights reserved.

−2/3 −2/3, and −1 −1 spots were almost the same as those for the 1/3 1/3, 2/3 2/3, and 1 1 spots, respectively. This means that the 3 × 3 structure of germanene has mirror symmetry with respect to the [1 1 $\bar{2}$] direction. Following this qualitative observation, the rocking curves were quantitatively analysed using the dynamical diffraction theory. The optimized result (figure 12(b)) shows that only one Ge atom, labelled 7 in the diagram, protrudes above the level of the other Ge atoms. The magnitude of the buckling of the Ge atom was determined to be 0.94 Å. The Al atom just below the protruding Ge atom is shifted upwards 0.42 Å from the level of the other Al atoms. The averaged spacing between the lower Ge layer and the first Al layer is estimated as 2.51 Å.

6.3. Super-structure of the rutile-TiO_2(1 1 0)-(1 × 2) surface

TiO_2 is widely used as a heterogeneous support for metal catalysts, as a catalyst for decontamination, sterilisation, and in solar cells. In addition, it is used as a standard material to test the catalytic processes of metal oxides that are important as catalytic or sensor materials [61, 62]. Knowledge of the structure of the surface is crucial for studying the fundamentals of the reactivity and reaction mechanisms of solid catalysts. As a testing ground for molecule- and metal-nanoparticle adsorptions, single-crystal TiO_2 surfaces have been studied extensively [63, 64].

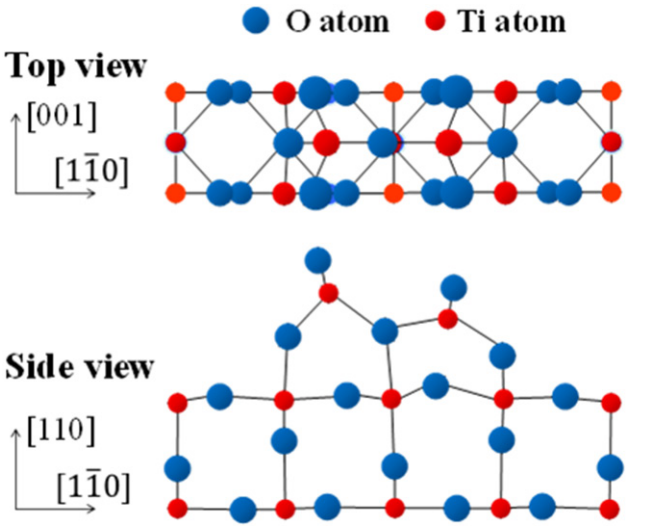

Figure 14. Rutile-TiO_2(1 1 0) (1 × 2) surface structure determined (asymmetric Ti_2O_3 model) [72]. Reproduced from [72]. CC BY 3.0.

A rutile-TiO_2 (1 1 0)-(1 × 1) surface, which is most stable with a well-known structure, turns into a rutile-TiO_2 (1 1 0)-(1 × 2) structure after heating to 1200 K. The structure is so complex that a detailed atomic configuration had not been settled some 30 years after its discovery [65], while many theoretical models were proposed [64, 66–71]. Thus, a conclusive determination of the structure was desired for further study of its property. With this aim, Mochizuki *et al* [72] analyzed the rocking curve of the 0 0 spot of the TRHEPD pattern of this surface. Results of the calculation of the rocking curve based on the atomic coordinates of any of the proposed models did not agree with the experimental results.

However, small adjustments in the coordinates of the model by Wang *et al* [71] gave good agreement (figure 14). This structure has the same chemical composition as the outermost structure given by the Ti_2O_3 model proposed by Onishi and Iwasawa [73], but with the symmetric constraint of the two Ti–O tetrahedra. Wang *et al* [71] reached this structure by a large calculation allowing for freedom in the composition and arrangement of atoms in their theoretical calculations using the ASPEX code.

7. Other applications of TRHEPD

The total reflection of positrons is useful not only for the determination of the surface structures but also for the studies of surface properties.

7.1. Surface phase transition of Si(1 1 1)-(√3 × √3) Ag

Noble-metal-atom adsorbed Si(1 1 1) surfaces exhibit various superstructures. One typical example is a Si(1 1 1)-(√3 × √3) Ag surface [74–76]. On depositing one monolayer of Ag atoms

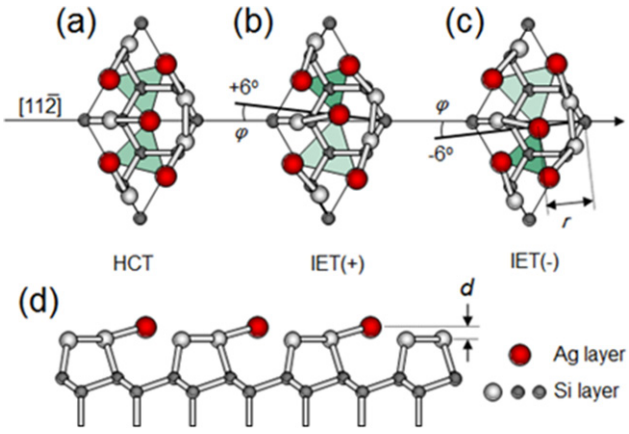

Figure 15. Ball and stick models (top view) of (a) honeycomb-chained-triangle (HCT) and inequivalent triangle (IET) structures ((b) IET(+) and (c) IET(−)) for the Si(1 1 1) ($\sqrt{3} \times \sqrt{3}$) Ag surface [80]. The side view is depicted in (d). Red and grey circles indicate Ag and Si atoms, respectively. φ, r, and d denote the cylindrical coordinates of the Ag atoms. Reprinted from [80], Copyright 2007 by the American Physical Society.

onto a Si(1 1 1)-(7 × 7) surface at around 770 K, the $\sqrt{3} \times \sqrt{3}$ structure appears. After a long-lasting controversy, its basic structure was recognized to be honeycomb-chained-triangle (HCT, figure 15(a)) by SXRD [77]. Then the detailed atomic configuration was settled to be the so-called inequivalent triangle (IET) structure [78, 79], as shown in figures 15(b) and (c). However, an issue concerning the phase transition remained explaining the difference between the scanning tunnelling microscopy images at room and low temperatures [78]. This issue has been addressed by TRHEPD [80], with the conclusion described below.

The open circles in figure 16 show the temperature dependence of TRHEPD intensities for 0 0, 1/3 1/3, and 2/3 2/3 spots measured in the temperature range from 48 K to 247 K. The phase transition temperature (T_c) was determined to be 123 K from the abrupt change in the temperature dependence of the intensity of the 1/3 1/3 spot. In contrast, interestingly the intensities of the 0 0 and 2/3 2/3 spots were nearly independent of temperature. These features cannot be explained by the effect of the Debye–Waller factor or the displacements of the topmost Ag atoms, but by considering the order–disorder phase transition of the IET structure.

The order parameter, p, in phase transition at temperature T below the critical temperature T_c is expressed in terms of the critical exponent β for the phase transition as

$$p \propto \left|1 - \frac{T}{T_c}\right|^{\beta}. \tag{19}$$

The IET structure has two different configurations with an equivalent surface energy, which are denoted by IET(+) and IET(−) in figure 15 [78]. The order parameter for the phase transition is written as

$$p = \frac{n_+ - n_-}{n_+ + n_-} = n_+ - n_-, \tag{20}$$

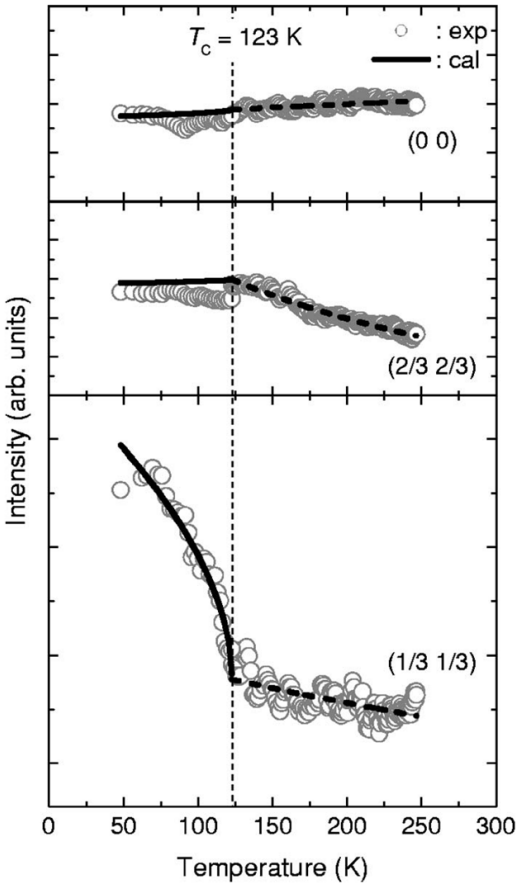

Figure 16. Temperature dependence of the TRHEPD spot intensities for the Si(1 1 1) ($\sqrt{3} \times \sqrt{3}$) Ag surface [80]. The incident positron energy was 10 keV. The glancing angle, 2.0°, is in the region of the total reflection. The incident azimuth was set at 1.5° off the [1 1 $\bar{2}$] direction. Open circles indicate the experimental curve. Solid line shows the calculated result using the optimum structure parameters. Reprinted from [80], Copyright 2007 by the American Physical Society.

where n_+ and n_- denote the occupation probabilities of the IET(+) and IET(−) structures, respectively, with $n_+ + n_- = 1$. When the domains with the anti-phase coexist, the TRHEPD intensity of the hk spot is expressed as

$$I_{\mathrm{hk}}^{\mathrm{total}}(p) = I_{hk}(p) + I_{hk}(-p). \tag{21}$$

Figure 17(a) shows the intensities of the 0 0, 1/3 1/3, and 2/3 2/3 spots as functions of p calculated on the basis of the dynamical diffraction theory. As p increases with decreasing T below T_c, the strong T dependence of the intensity of the 1/3 1/3 spot shown in figure 16 is consistent with the order–disorder transition explanation of its temperature dependence.

The origin of the index-dependent intensity change with p is understood in terms of the kinematical approximation. In this approximation, the structure factor, $F(p)$, is expressed simply as

$$F(p) = \frac{1+p}{2}F_+ + \frac{1-p}{2}F_-, \tag{22}$$

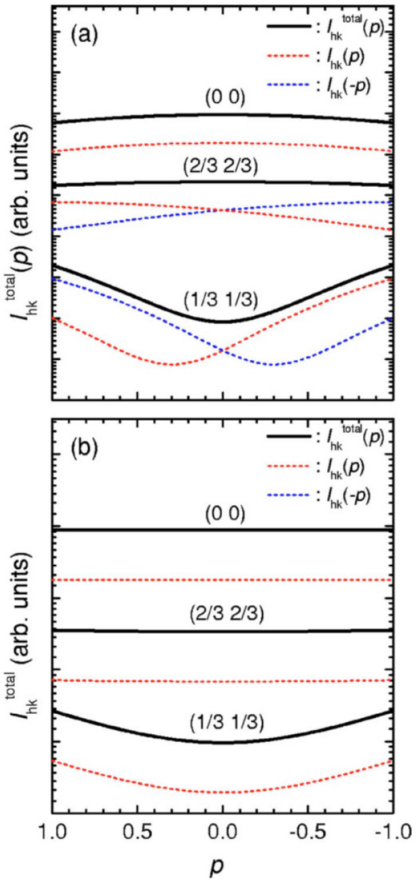

Figure 17. TRHEPD intensity of the spots indicated for the Si(1 1 1) ($\sqrt{3} \times \sqrt{3}$) Ag surface calculated as functions of the order parameter (p) on the basis of (a) dynamical and (b) kinematical diffraction theories [80]. The incident conditions are described in the text. Red and blue dotted lines indicate the contributions from p and $-p$, respectively. Solid lines show the total intensities. In (b), the blue lines cannot be seen as they overlap with the red lines. Reprinted from [80], Copyright 2007 by the American Physical Society.

where F_+ and F_- indicate the structure factors for IET(+) and IET(−), respectively. Since the atomic configurations of the IET(+) and IET(−) structures leads to the relation $F_+ = F_-^*$ ($F_- = F_+^*$), where $*$ indicates the complex conjugate, the total intensity is written as

$$I_{\mathrm{hk}}^{\mathrm{total}}(p) = |F(p)|^2 + |F(-p)|^2 = 2\,\mathrm{Re}\,(F_+)^2 + 2p^2\,\mathrm{Im}\,(F_+)^2. \tag{23}$$

The resulting total intensities of the spots are shown in figure 17(b). The atomic configurations of the IET(+) structure gives the relation $|\mathrm{Re}(F_+)| \cong |\mathrm{Im}(F_+)|$ for the 1/3 1/3 spot, leading to a nearly parabolic dependence on p. On the other hand, the relation $|\mathrm{Re}(F_+)| > |\mathrm{Im}(F_+)|$ holds for the 0 0 and 2/3 2/3 spots and thus the intensities are almost constant against p. The weak p dependence of the intensities for 0 0 and 2/3 2/3 spots explains their insensitivity to the phase transition.

The value of β was determined to be 0.28 ± 0.05 by minimizing the difference between the measured and calculated intensities for the 1/3 1/3 spot, as shown in figure 16. The value is consistent with the result of SXRD [79] and is intermediate between those for the 2D (0.125) and 3D Ising systems (~0.325). This implies that in regard to the phase transition, the Si(1 1 1)-($\sqrt{3} \times \sqrt{3}$) Ag surface is not a pure 2D system.

7.2. Surface Debye temperature

The temperature dependence of the TRHEPD spot intensities provides a reliable method for the determination of the surface Debye temperatures. In order to see the sensitivity of this method, the temperature dependence of the TRHEPD intensities of the 0 0 and 1 1 spots from the Si(1 1 1)-(7 × 7) surface were calculated for various values of incident glancing angle θ and azimuthal angle, φ, which is defined as the angle from the $[1\,1\,\bar{2}]$ direction [81]. The energy of the incident positrons was $E = 20$ keV, for which the critical angle of the total reflection is 1.4°. Figure 18(a) shows the results of the calculations for two different values, 300 K and 600 K, of the bulk Debye temperature (Θ_B), made by assuming that the surface Debye temperature (Θ_S) is 300 K. Here, the surface atoms are considered to be those down to the second layer and the bulk is from the third layer and below. The result shows, as expected, that the intensities for the 0 0 and 1 1 spots for $\theta = 1.0°$, in the total reflection condition, and for $\theta = 1.6°$, slightly above the critical angle, were independent of Θ_B. The feature was also seen for the 1 1 spot under the total reflection condition at a different incident azimuth. For $\theta = 3.5°$, well outside the total reflection condition, the results for $\Theta_B = 300$ K and 600 K are quite different from each other. These results demonstrate that it is possible without a detailed knowledge of Θ_B to determine Θ_S accurately from the temperature dependence of the TRHEPD intensity under the total reflection condition.

Figure 18(b) shows the results of measurements on a Si(1 1 1)-(7 × 7) surface. The closed squares indicate the obtained temperature dependences of the TRHEPD intensities of the 0 0 and 1 1 spots at various glancing angle. The experimental conditions were the same as used in the calculations shown in figure 18(a). The value of Θ_S was determined from the fitting of the 1 1 spot intensity at $\theta = 1.0°$ and $\varphi = 1.5°$ in terms of the reliability factor, R, defined as (figure B1) in appendix B. The optimized value was found to be 290 K. The corresponding root mean square of the vibrational amplitude at room temperature is 0.14 Å, much larger than that estimated in a previous report [82] using RHEED technique. The present value amounts to a vibrational energy of 25 meV, agreeing with the vibrational modes related to the adatoms estimated from electron energy-loss spectroscopy [83]. Once Θ_S is determined, the value of Θ_B is deduced from fitting to the intensity at $\theta = 3.5°$ and $\varphi = 7.5°$, in which condition the positrons can penetrate in the bulk. The value determined from the minimum of R was $\Theta_B = 600$ K. The value is consistent with the literature [84]. The large difference in Θ_S and Θ_B indicates that the vibrational amplitude at the surface is much enhanced compared to that in the bulk.

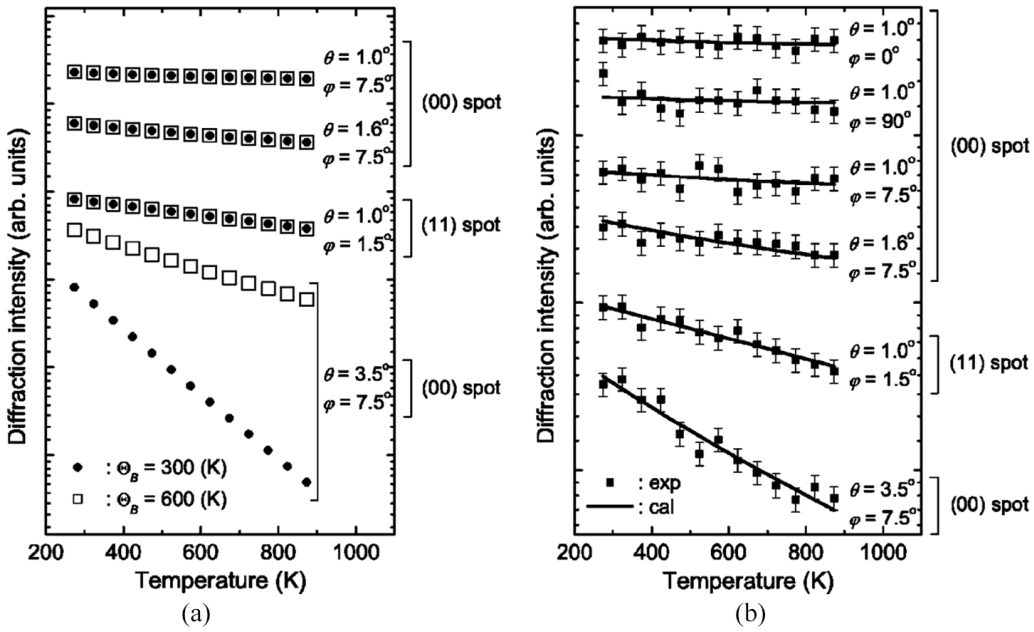

Figure 18. (a) Temperature dependence of the TRHEPD intensity calculated for a Si(1 1 1) (7 × 7) surface with incident glancing angle θ and azimuth angle, φ, measured from the $[1\,1\,\bar{2}]$ direction. The incident positron energy is 20 keV. The critical angle for the total reflection is $\theta_c = 1.4°$. Circles and squares indicate, respectively, the intensities calculated using $\Theta_B = 300$ K and $\Theta_B = 600$ K with fixed $\Theta_S = 300$ K. (b) Measured temperature dependence of the TRHEPD intensity from the Si(1 1 1) (7 × 7) surface in the same experimental conditions as for the calculations in (a). Solid lines show the intensities calculated for the optimized values $\Theta_S = 290$ K and $\Theta_B = 600$ K. Reprinted from [81], Copyright 2004 by the American Physical Society.

7.3. Plasmon excitations

The electronic excitation resulting from surface plasmons is a dominant inelastic process for positron diffraction. Positron energy loss spectra were measured with an analyser composed of mesh electrodes [16].

Figure 19(a) shows the energy loss spectra of the positron and electron beams from the Si(1 1 1)-(7 × 7) surface [16]. The incident glancing angles are 1.5° (in the total reflection region) for positrons and 1.3° for electrons. The spectrum for the positron has much more distinct step structures than that for the electron. Figures 19(b) and (c) represent smoothed differential curves of the spectra for the positron and the electron, respectively. The peaks appear with an interval of ~11 eV. The energy loss is expressed as $E_{\mathrm{loss}} = n\hbar\omega$, where $\hbar\omega$ is the plasmon energy and n is the number of the plasmon excitations. The peaks observed in figure 19(b) correspond to $n = 0$ to 5. The maximum of the peak intensity corresponds to larger excitation number (energy loss) for the positron than for the electron. The expectation number of the excited plasmons, $P(n)$, is described by the Poisson distribution [85]

$$P(n) = \frac{n_s^n \exp(-n_s)}{n!}, \tag{24}$$

where n_s denotes the mean excitation number of surface plasmons. By fitting the envelope curves of the peaks of the spectra shown in figure 19 to equation (24), $n_s = 2.6$ (positron) and $n_s = 1.4$ (electron) were obtained. The latter was consistent with previous studies [86–89]. Thus, the mean excitation number for positrons is about twice as large as that for electrons.

The excitation of the surface plasmons leads to the broadening of the spot profile. The circles in figure 20 represent the profile of the 0 0 spot from the Si(1 1 1)-(7 × 7) surface at $\theta = 2.0°$, deconvoluted for the incident positron beam profile. For a single surface plasmon excitation, the spot profile is expressed to be [89, 90]

$$I_1\left(\theta_{\parallel},\, \theta_{\perp}\right) \propto \frac{\sqrt{\left(\theta_{\parallel}/\theta_E\right)^2+1}}{\left[\left(\theta_{\parallel}/\theta_E\right)^2+\left(\theta_{\perp}/\theta_E\right)^2+1\right]^2}, \tag{25}$$

where $\theta_{\parallel}$ and $\theta_{\perp}$ are the cone angle from the beam centre to the azimuthal and glancing angle directions, respectively, and $\theta_E = \hbar\omega/2E$, E being the positron beam energy. The surface-parallel and the surface-normal components of the wave number k are expressed as $k_{\parallel} = k\sin\theta_{\parallel}$ and $k_{\perp} = k\sin\theta_{\perp}$, respectively. For double excitations, the profile is expressed by a self-convolution of (25) as $I_2\left(\theta_{\parallel}, \theta_{\perp}\right) = I_1\left(\theta_{\parallel}, \theta_{\perp}\right) \otimes I_1\left(\theta_{\parallel}, \theta_{\perp}\right)$. Generally, for n-fold excitations, the profile is given by

$$I_n\left(\theta_{\parallel}, \theta_{\perp}\right) = I_{n-1}\left(\theta_{\parallel}, \theta_{\perp}\right) \otimes I_1\left(\theta_{\parallel}, \theta_{\perp}\right). \tag{26}$$

Figure 20(b) exhibits the spot profile at each excitation, calculated using (25). With increasing excitation number for the surface plasmons, the spot becomes wider. The observed

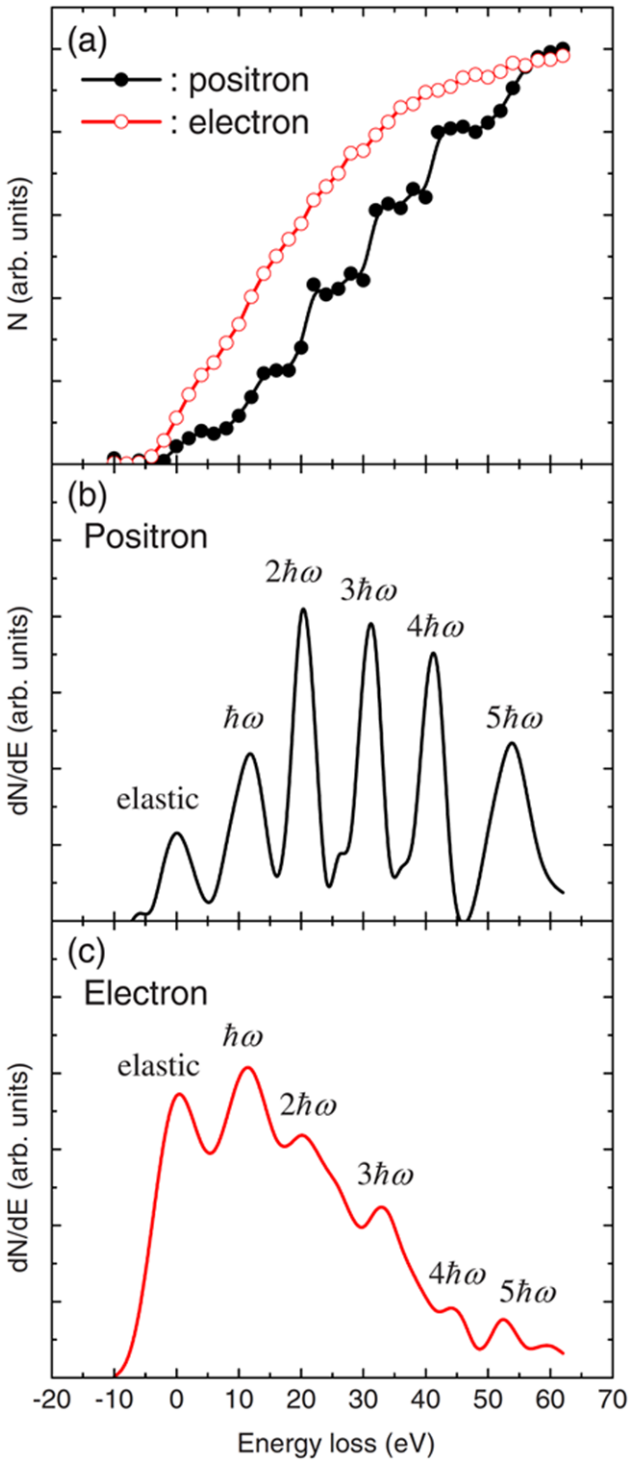

Figure 19. (a) Measured energy loss spectra of positrons (closed circles) and electrons (open circles) for the Si(1 1 1)-(7 × 7) surface and the differential of the spectra for (b) positrons and (c) electrons. Reprinted from [16], Copyright 2009 by the American Physical Society.

spot profile is given by the sum of the products of (24) and (26) as

$$I\left(\theta_{\parallel},\theta_{\perp}\right)=\sum_{n} I_{n}\left(\theta_{\parallel},\theta_{\perp}\right)P\left(n\right). \tag{27}$$

As shown by the red line in figure 20(a), the calculated profile using $n = 2.6$, reproduces the experimental one very well.

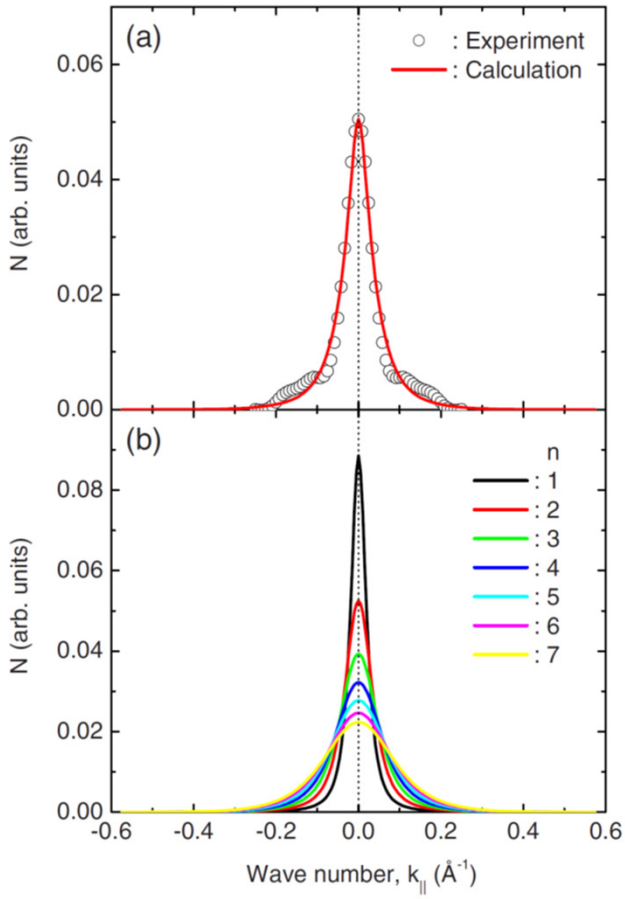

Figure 20. (a) Profile of the specular spot for the Si(1 1 1)-(7 × 7) surface [16]. Open circles represent the experimental profile. Solid line shows the calculated profile with the multiple excitations of the surface plasmon taken into account. (b) Spot profile calculated using equation (25) for each n. The horizontal axis was transformed from the angle to the wave number using the relation $k_{\parallel} = k \sin\theta_{\parallel}$. Reprinted from [16], Copyright 2009 by the American Physical Society.

8. Summary

It has been about two and a half decades since (T)RHEPD was proposed and two decades since the first diffraction pattern was obtained. The present review describes the surface sensitivity of TRHEPD and some of the surface structures such as atomic nanowires, single atomic sheet materials and catalysts. Some applications focusing on surface phase transitions, surface phonons and surface plasmons that take advantage of the total-reflection characteristic of the positron are also described.

Acknowledgments

We thank M Maekawa, I Mochizuki, K Wada and T Shidara for their support in the construction of the apparatus, experimental work and discussions. We also thank T Takahashi for valuable discussions. This work was partly conducted under PF Proposal No. 2010G652, 2012G653, 2013U002, 2014S2-004, and the auspices of the Joint Development Research at

the High Energy Accelerator Research Organization (KEK). The present work was partly supported by a Grant-in-Aid for Scientific Research (S) 24221007 and for Young Scientists (B) 25800182 from JSPS.

Appendix A. Preparation of slow positron beams

In both radioisotope- and linac-based beams, primary positrons have a very wide energy distribution. The upper limit of the energy depends on the specific β^+ decay (up to a few MeV) and the acceleration energy of the linac (up to a few tens of MeV). Thus, the first step to create a slow positron beam suitable for TRHEPD is to make a mono-energetic beam. It is not efficient to use a spectroscopic method to select positrons in a narrow range of energy and directions. Fortunately, a much more efficient method has been developed [24–26, 91], which relies on metals whose work function for positrons is negative. A small fraction of the positrons that are thermalized in such metals, diffuse back to the surface before annihilation and are spontaneously emitted out with an energy equal to the absolute value of the work function and the width of the thermal energy. Typical metals of this kind are W, Cu and Ni, with work functions of about -3 eV, -0.3 eV and -1 eV, respectively [91]. The positrons are then accelerated to an energy suitable for experiment and transportation to the measurement chamber. Electrostatic and magnetic transportation systems are both in practice. The transported beam must be released into a field-free space before entering the diffraction chamber.

In the early stages of (T)RHEPD experiments, positrons emitted from the β^+ decay of a radioisotope ^{22}Na were used [8, 9, 92]. Although the flux of the obtained slow positron beam was very small (one fA or less), TRHEPD experiments were successfully performed due to the high reflectivity of positrons in total reflection and an effective use of the analysis of the rocking curves for the intense 0 0 spot [9].

We describe here two radioactive-source based beams developed at JAEA and a linac-based beam at KEK.

A.1. Radioisotope-based slow-positron beams

The first TRHEPD (then called RHEPD) apparatus was realized at JAEA, in Takasaki [8, 92]; its positron gun consisting of a ^{22}Na positron source (<5 mCi), a well-annealed W moderator (500 nm thick), an extraction grid, a Wehnelt electrode, a Soa tube and an anode [93]. The reemission energy of the positron was 3 eV with an energy width of the thermal energy.

The positrons were transported electrostatically with three einzel lenses. The source and the electrodes down to the first einzel lens were electrostatically floated against the grounded downstream portion including the sample. The bias voltages of each of the components were adjusted to give maximum positron flux for the 20 keV beam. Before entering the diffraction chamber, the beam was deflected by 3° and only the near axis-beam was selected by a long

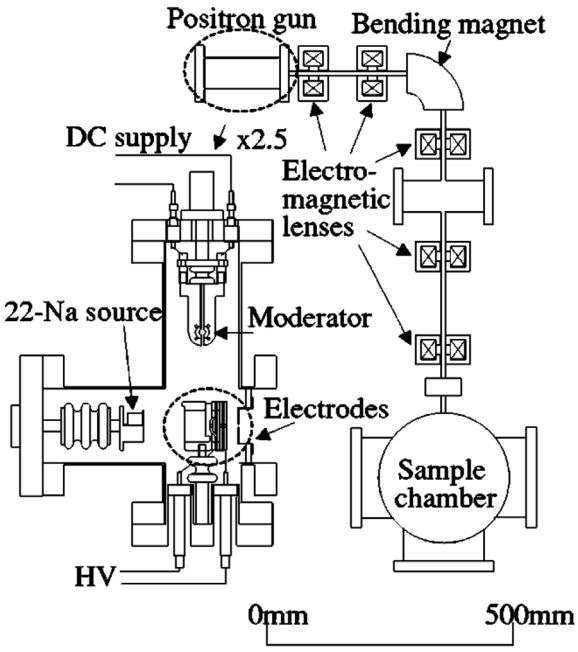

Figure A1. Schematic diagram of the TRHEPD apparatus with five electromagnetic lenses and a bending magnet. Reprinted from [94], Copyright 2004 AIP Publishing.

pipe-collimator ($\phi = 0.87$ m, $l = 140$ mm). This procedure reduced (improved) emittance of the beam at the expense of the beam intensity, hence with roughly conserved brightness.

The final beam intensity was $I \sim 5 \times 10^3$ positrons/s (~ 1 fA), Note that the improvement of the emittance is essential for the diffraction experiments. The weak beam intensity demanded long measurement times; more than 4 h were required to obtain an image of the specular spot on a phosphor screen at the back of a microchannel plate assembly (MCPA) with a CCD camera.

The second (T)RHEPD apparatus constructed at JAEA is shown in figure A1 [94]. Positrons from a 3.7 GBq (100 mCi) ^{22}Na source were moderated by a W(1 0 0) single crystal moderator of thickness 500 nm. The positron gun consisted of an extractor, a Wehnelt electrode, a Soa tube and an anode. The electrostatic potential of the ^{22}Na source was 10 kV. The anode was grounded and the other electrodes were appropriately biased.

Instead of the electrostatic lenses, as in the first apparatus, five electromagnetic lenses were employed. A 90° bending magnet of 75 mm curvature radius with steering coils selected the positrons of a fixed energy (10 keV). The objective lens focused the beam on a grounded sample on a five-axis PC-controlled manipulator in the TRHEPD experiment chamber. The diameter of the remoderated positron beam at the sample position was about 0.5 mm full width at half maximum (FWHM). With a source activity of 3.7 GBq, the final beam flux was $I \sim 2 \times 10^4$ positrons/s (~ 3 fA), and the brightness was $B \sim 10^7$ e$^+$/(s cm^2 rad^2 V) (see section A.3 below). The coherence lengths parallel and normal to the beam direction were $l_p \sim 12$ nm and $l_n \sim 4$ nm.

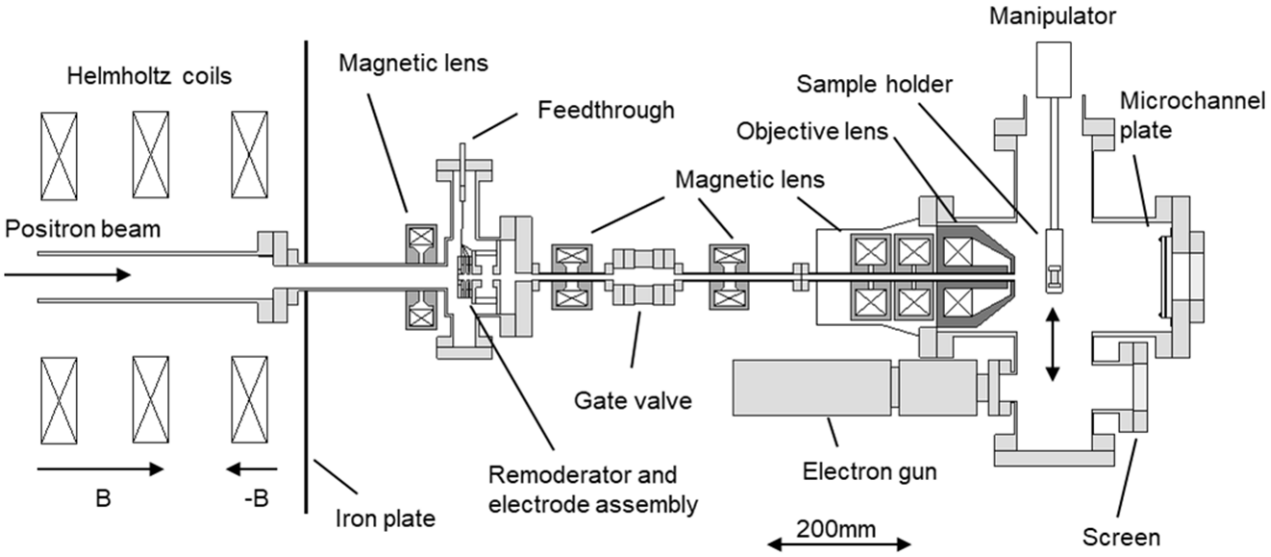

Figure A2. Schematic drawing of the TRHEPD apparatus using the linac-based positron beam [11]. The transmission-type brightness enhancement system is composed of the remoderator and the electrode assembly, installed upstream of the TRHEPD chamber. Reprinted by permission from [11]. © 2014, EDP Sciences, SIF, Springer-Verlag Berlin Heidelberg. With permission of Springer.

A.2. Linac-based slow positron beam

In the linac-based slow positron beam at the Slow Positron Facility (SPF), IMSS, KEK [10, 13], a pulsed 50 Hz electron beam generated with a dedicated linac (operated at ~50 MeV, 0.6 kW) is impacted onto a 4 mm thick Ta converter where Bremsstrahlung radiation creates electron–positron pairs. A small fraction of the created positrons are thermalized in a W foil moderator, diffuse back to the surface of the foil and then reemitted into the free space with an energy 3 eV, as in the case of the radioisotope-based beam. The positron converter/moderator assembly can be held at a variable electrostatic voltage (0–35 kV), normally set at 15 kV for TRHEPD measurements. The emitted positrons are thus accelerated to 15 keV into the grounded beam-line and are guided by a magnetic field of about 0.015 T.

A.3. Brightness enhancement

Figure A2 shows the end of the magnetically guided beam-line, brightness-enhancement unit and the TRHEPD measurement chamber [11]. The principle of brightness enhancement is the same as that of moderation of the initial high-energy positrons. Thus, brightness enhancement is often called remoderation.

The beam brightness is defined as [25, 26, 95]

$$B = \frac{I}{\varepsilon_{norm}^2} = \frac{I}{\varepsilon^2 E} = \frac{I}{r^2\theta^2 E}, \tag{A.1}$$

where I is the beam flux, E the beam energy, r the beam radius (half width at half maximum, HWHM) and θ the beam divergence (HWHM). $\varepsilon_{norm}(=\varepsilon\sqrt{E})$ is called the normalized emittance, where $\varepsilon(=r\theta)$ is the beam emittance defined as area in terms of the particle position and the angle in radians occupied by the beam particles divided by π.

For TRHEPD measurements, the transported beam must be released into a field-free region. In the linac-based beam at KEK, the transporting magnetic flux density is terminated by a reversed magnetic field produced by the final magnetic coil and an iron plate. The 15 keV beam is then focused onto a transmission-type remoderator (100 nm W film) [96–98] held at an electrostatic potential of 10 kV. With a 5 keV incident energy, about 10% of the positrons are thermalized in the W film and reemitted from the back. Change in the beam parameters across the film are: beam intensity from 1×10^7 e^+/s to 1×10^6 e^+/s (~0.1 pA), beam divergence from ~50° to ~10°, and beam energy from 5 keV to 3 eV. The beam diameter of ~ 0.75 mm is unchanged. Thus the normalized emittance is reduced to 10^{-4}, making the brightness enhanced by 10^3. The resulting brightness is estimated to be $B \sim 6 \times 10^9$ e^+/(s cm^2 rad^2 eV). Since the remoderator film is electrically set at 10 kV, the kinetic energy of the remitted positrons on the grounded sample is 10 keV.

The coherence lengths of the final beam along and normal to the beam are represented (in nm) as

$$l_p = \frac{1}{\sqrt{\left(\frac{\Delta E}{2.45\sqrt{E}}\right)^2 + \left(\frac{\theta \sin\theta_g}{\lambda}\right)^2}} \tag{A.2}$$

$$l_n = \frac{\lambda}{\Delta\theta}, \tag{A.3}$$

respectively [99], where E is energy in eV, θ_g the glancing angle, $\Delta\theta$ the angular uncertainty, and λ the wavelength of the beam. The estimated coherence lengths of the beam are $l_P \sim$ 30 nm and $l_n \sim$ 1 nm, respectively.

The diffraction patterns are intensified using a microchannel plate (MCP) with a phosphor screen, recorded with a charge coupled device (CCD) camera and then stored in a personal computer. The rocking curves are measured by rotating the sample up to $\theta = 6°$ in steps of 0.1° using a stepping motor, which was controlled by the personal computer.

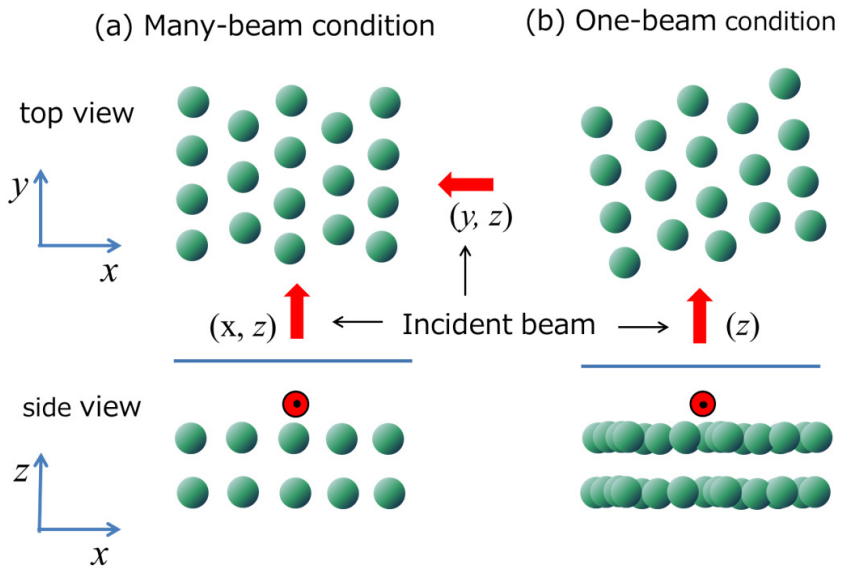

Figure B1. Schematic illustration of (a) many-beam condition and (b) one-beam condition.

Appendix B. Rocking curve analysis of the TRHEPD patterns

Practically, the rocking curves, or the incident glancing angle dependence, of the intensity of a spot (typically 0 0 or specular spot, but also others) are analyzed. An experimental rocking curve is essentially the same as the experimental reflectivity shown in figure 4, except that the former usually represents the intensity of the spot as measured and the calculated curve includes the glancing factor, $\sin\theta$, of the sample surface, while the latter is corrected for the glancing factor.

The rocking curve of the intensity of the 0 0 spot is extracted from each pattern measured for a glancing angle of up to $\theta = 6°$, usually in steps of 0.1°. The data are stored in a personal computer. The intensity of the 0 0 spot in the TRHEPD pattern is so high that it takes only 2 min or so to obtain sufficient data for the rocking curve analysis at each glancing angle.

Figure B1 illustrates two different incident conditions used in the rocking curve analysis. The diffraction pattern for a positron beam with energy 10 keV is sensitive to the coordinates of the atoms perpendicular to the direction of the incident beam only. The setting shown in figure B1(a) is called a many-beam condition, where the beam is directed along a symmetric direction of the atomic arrangement on the surface. In this condition, the diffraction pattern is sensitive to the atomic coordinate normal to the surface (z) and one of the in-plane coordinates (x). Information on the other in-plane coordinate (y) is obtained from measurement at another incident direction. The setting shown in figure B1(b) is called a one-beam condition [100], where the beam is directed from a direction off the many beam direction by an appropriate angle so that essentially no in-plane diffraction takes place. When the structure of the (1 1 1) surface of an fcc crystal is studied, for example, the [1 1 $\bar{2}$] and [1 $\bar{1}$ 0] directions are chosen for the many-beam condition, then the one-beam condition is set 13° off the [1 1 $\bar{2}$] direction.

In the analysis of the rocking curves, the data under the one-beam condition is analysed first because this allows the determination of the surface-normal coordinates of the atoms without consideration of the in-plane coordinates. Then, with the knowledge of the surface-normal coordinates of the atoms already determined, the in-plain coordinates are obtained from the data under many-beam conditions.

In practice, a structural model is assumed, the expected rocking curve is calculated and the goodness of fit with the experimental data is checked in terms of the reliability factor, R, defined as

$$R = \sqrt{\sum_{\theta} \left(I_{\theta}^{\mathrm{exp}} - I_{\theta}^{\mathrm{cal}}\right)^2}, \tag{B.1}$$

where $I_{\theta}^{\mathrm{exp}}$ and $I_{\theta}^{\mathrm{cal}}$ are the spot intensities of the experiment and the calculation at θ, respectively [81]. They are normalized to $\sum_{\theta} I_{\theta}^{\mathrm{exp}} = \sum_{\theta} I_{\theta}^{\mathrm{cal}} = 1$ or 100 %.

The uncertainty of the value of a coordinate of each atom from a typical measurement at KEK is about 0.05Å. It is estimated as follows using rocking curve data from a number of runs with the same measurement condition [72]. First, the standard deviation of the R values for the runs, ΔR, is calculated. Then, R-like value is calculated with replacing, in (B.1), $I_{\theta}^{\mathrm{cal}}$ by the rocking-curve for the best fit structure and $I_{\theta}^{\mathrm{exp}}$ by that for the structure where a coordinate, say z, of the atom in question alone deviates by Δz from that of the best fit structure. The value of Δz, which makes the R-like value increase by ΔR, is assigned as the uncertainty of z for the atom in question.

ORCID iDs

Toshio Hyodo https://orcid.org/0000-0002-1810-732X

References

[1] Pendry J B 1974 *Low Energy Electron Diffraction* (New York: Academic)
[2] Ichimiya A and Cohen P I 2004 *Reflection High-Energy Electron Diffraction* (Cambridge: Cambridge University Press)
[3] Robinson I K and Tweet D J 1992 *Rep. Prog. Phys.* **55** 599
[4] Rosenberg I J, Weiss A H and Canter K F 1980 *Phys. Rev. Lett.* **44** 1139
[5] Tong S Y, Huang H and Guo X Q 1992 *Phys. Rev. Lett.* **69** 3654
[6] Wu H and Tong S Y 2001 *Phys. Rev. Lett.* **87** 036101
[7] Ichimiya A 1992 *Solid State Phenom.* **28&29** 143
[8] Kawasuso A and Okada S 1998 *Phys. Rev. Lett.* **81** 2695
[9] Fukaya Y, Maekawa M, Mochizuki I, Wada K, Hyodo T and Kawasuso A 2013 *J. Phys.: Conf. Ser.* **443** 012068
[10] Wada K *et al* 2012 *Eur. Phys. J.* D **66** 37
[11] Maekawa M, Wada K, Fukaya Y, Kawasuso A, Mochizuki I, Shidara T and Hyodo T 2014 *Eur. Phys. J.* D **68** 165
[12] Fukaya Y, Maekawa M, Kawasuso A, Mochizuki I, Wada K, Shidara T, Ichimiya A and Hyodo T 2014 *Appl. Phys. Express* **7** 056601
[13] Hyodo T *et al* 2017 *J. Phys.: Conf. Ser.* **791** 012003
[14] Hugenschmidt C 2016 *Surf. Sci. Rep.* **71** 547
[15] Parratt L G 1954 *Phys. Rev.* **95** 359
[16] Fukaya Y, Kawasuso A and Ichimiya A 2009 *Phys. Rev.* B **79** 193310
[17] Maksym P A and Beeby J L 1981 *Surf. Sci.* **110** 423
[18] Ichimiya A 1983 *Japan. J. Appl. Phys.* **22** 176
Ichimiya A 1985 *Japan. J. Appl. Phys.* **24** 1365
[19] Bird D M and King Q A 1990 *Acta Crystallogr.* A **46** 202
[20] Doyle P A and Turner P S 1968 *Acta Crystallogr.* A **26** 390
[21] Dudarev S L, Peng L-M and Whelan M J 1995 *Surf. Sci.* **330** 86
[22] Radi G 1970 *Acta Crystallogr.* A **26** 41
[23] Woodruff D P and Delchar T A 1994 *Modern Techniques of Surface Science* (Cambridge: Cambridge University Press)
[24] Mills A P Jr, Platzman P M and Brown B L 1978 *Phys. Rev. Lett.* **41** 1076
[25] Mills A P Jr 1983 *Positron Solid-State Physics* ed W Brandt and A Dupasquier (Amsterdam: North-Holland) p 432
[26] Schultz P J and Lynn K G 1988 *Rev. Mod. Phys.* **60** 701
[27] Takayanagi K, Tanishiro Y, Takahashi S and Takahashi M 1985 *Surf. Sci.* **164** 367
[28] Brommer K D, Needels M, Larson B E and Joannopoulos J D 1992 *Phys. Rev. Lett.* **68** 1355
[29] Gürlu O, Adam O A O, Zandvliet H J W and Poelsema B 2003 *Appl. Phys. Lett.* **83** 4610
[30] van Houselt A, Gnielka T, Aan de Brugh J M J, Öncel N, Kockmann D, Heid R, Bohnen K P, Poelsema B and Zandvliet H J W 2008 *Surf. Sci.* **602** 1731
[31] Stekolnikov A A, Bechstedt F, Wisniewski M, Schäfer J and Claessen R 2008 *Phys. Rev. Lett.* **100** 196101
[32] Stekolnikov A A, Furthmüller J and Bechstedt F 2008 *Phys. Rev.* B **78** 155434
[33] Vanpoucke D E P and Brocks G 2008 *Phys. Rev.* B **77** 241308
[34] Vanpoucke D E P and Brocks G 2010 *Phys. Rev.* B **81** 085410
[35] Mochizuki I, Fukaya Y, Kawasuso A, Yaji K, Harasawa A, Matsuda I, Wada K and Hyodo T 2012 *Phys. Rev.* B **85** 245438
[36] Schwingenschlogla U and Schuster C 2008 *Europhys. Lett.* **81** 26001
[37] Geim A K 2009 *Science* **324** 1530
[38] Ezawa M 2015 *J. Phys. Soc. Japan* **84** 121003
[39] Cahangirov S, Topsakal M, Aktürk E, Şahin H and Ciraci S 2009 *Phys. Rev. Lett.* **102** 236804
[40] Lin C-L, Arafune R, Kawahara K, Kanno M, Tsukahara N, Minamitani E, Kim Y, Kawai M and Takagi N 2013 *Phys. Rev. Lett.* **110** 076801
[41] Vogt P, De Padova P, Quaresima C, Avila J, Frantzeskakis E, Asensio M C, Resta A, Ealet B and Le Lay G 2012 *Phys. Rev. Lett.* **108** 155501
[42] Lin C-L, Arafune R, Kawahara K, Tsukahara N, Minamitani E, Kim Y, Takagi N and Kawai M 2012 *Appl. Phys. Express* **5** 045802
[43] Fukaya Y, Mochizuki I, Maekawa M, Wada K, Hyodo T, Matsuda I and Kawasuso A 2013 *Phys. Rev.* B **88** 205413
[44] Dlubak B *et al* 2012 *Nat. Phys.* **8** 557
[45] Giovannetti G, Khomyakov P A, Brocks G, Karpan V M, van den Brink J and Kelly P J 2008 *Phys. Rev. Lett.* **101** 026803
[46] Batzill M 2012 *Surf. Sci. Rep.* **67** 83
[47] Eom D, Prezzi D, Rim K T, Zhou H, Lefenfeld M, Xiao S, Nuckolls C, Hybertsen M S, Heinz T F and Flynn G W 2009 *Nano Lett.* **9** 2844
[48] Silvestrelli P L and Ambrosetti A 2015 *Phys. Rev.* B **91** 195405
[49] Fukaya Y, Entani S, Sakai S, Mochizuki I, Wada K, Hyodo T and Shamoto S 2016 *Carbon* **103** 1–4
[50] Vanin M, Mortensen J J, Kelkkanen A K, Garcia-Lastra J M, Thygesen K S and Jacobsen K W 2010 *Phys. Rev.* B **81** 081408
[51] Gong C, Lee G, Shan B, Vogel E M, Wallace R M and Cho K 2010 *J. Appl. Phys.* **108** 123711
[52] Li L, Lu S-Z, Pan J, Qin Z, Wang Y-Q, Wang Y, Cao G-Y, Du S and Gao H-J 2014 *Adv. Mater.* **26** 4820
[53] Dávila M E, Xian L, Cahangirov S, Rubio A and Le Lay G 2014 *New J. Phys.* **16** 095002
[54] Bampoulis P, Zhang L, Safaei A, van Gastel R, Poelsema B and Zandvliet H J W 2014 *J. Phys.: Condens. Matter* **26** 442001
[55] Derivaz M, Dentel D, Stephan R, Hanf M-C, Mehdaoui A, Sonnet P and Pirri C 2015 *Nano Lett.* **15** 2510
[56] Acun A *et al* 2015 *J. Phys.: Condens. Matter* **27** 443002
[57] Zhang L, Bampoulis P, Rudenko A N, Yao Q, van Houselt A, Poelsema B, Katsnelson M I and Zandvliet H J W 2016 *Phys. Rev. Lett.* **116** 256804
[58] Stephan R, Hanf M C, Derivaz M, Dentel D, Asensio M C, Avila J, Mehdaoui A, Sonnet P and Pirri C 2016 *J. Phys. Chem.* C **120** 1580
[59] Liu G, Liu S B, Xu B, Ouyang C Y, Song H Y, Guan S and Yang S A 2015 *J. Phys. Chem. Lett.* **6** 4936
[60] Fukaya Y, Matsuda I, Feng B, Mochizuki I, Hyodo T and Shamoto S 2016 *2D Mater.* **3** 035019
[61] Fujishima A, Zhang X and Tryk D A 2008 *Surf. Sci. Rep.* **63** 515
[62] Henderson M A 2011 *Surf. Sci. Rep.* **66** 185
[63] Asakura K 2012 *Catalysis* vol 24 eds J J Spivey and M Gupta (Cambridge: RSC Publishing) p 281
[64] Diebold U 2003 *Surf. Sci. Rep.* **48** 53
[65] Cao C C, Tsai S C, Dahl M K, Chung Y W and Lo W J 1980 *Surf. Sci.* **95** 1
[66] Ng K-O and Vanderbilt D 1997 *Phys. Rev.* B **56** 10544
[67] Pang C L, Haycock S A, Raza H, Murray P W, Thornton G, Gülseren O, James R and Bullett D W 1998 *Phys. Rev.* B **58** 1586
[68] Blanco-Rey M, Abad J, Rogero C, Mendez J, Lopez M F, Martin-Gago J A and de Andres P L 2006 *Phys. Rev. Lett.* **96** 055502
[69] Elliott S D and Bates S P 2001 *Surf. Sci.* **495** 211
[70] Ünal H, Mete E and Ellialtıoğlu Ş 2011 *Phys. Rev.* B **84** 115407
[71] Wang Q, Oganov A R, Zhu Q and Zhou X F 2014 *Phys. Rev. Lett.* **113** 266101

[72] Mochizuki I, Ariga H, Fukaya Y, Wada K, Maekawa M, Kawasuso A, Shidara T, Asakura K and Hyodo T 2016 *Phys. Chem. Chem. Phys.* **18** 7085
[73] Onishi H and Iwasawa Y 1994 *Surf. Sci.* **313** L783
[74] Spiegel K 1967 *Surf. Sci.* **27** 125
[75] Le Lay G, Manneville M and Kern R 1978 *Surf. Sci.* **72** 405
[76] Gotoh Y and Ino S 1978 *Japan J. Appl. Phys.* **17** 2097
[77] Takahashi T, Nakatani S, Okamoto N, Ishikawa T and Kikuta S 1988 *Japan. J. Appl. Phys.* **27** L753
[78] Aizawa H, Tsukada M, Sato N and Hasegawa S 1999 *Surf. Sci.* **429** L509
[79] Tajiri H, Sumitani K, Nakatani S, Nojima A, Takahashi T, Akimoto K, Sugiyama H, Zhang X and Kawata H 2003 *Phys. Rev.* B **68** 035330
[80] Fukaya Y, Kawasuso A and Ichimiya A 2007 *Phys. Rev.* B **75** 115424
[81] Fukaya Y, Kawasuso A, Hayashi K and Ichimiya A 2004 *Phys. Rev.* B **70** 245422
[82] Fukaya Y, Nakamura K and Shigeta Y 2000 *J. Vac. Sci. Technol.* A **18** 968
[83] Daum W, Ibach H and Müller J E 1987 *Phys. Rev. Lett.* **59** 1593
[84] MacGillavry C H and Rieck G D ed 1968 *International Tables for X-Ray Crystallography* vol III (Birmingham: Kynoch Press)
[85] Lucas A A and Šunjić M 1971 *Phys. Rev. Lett.* **26** 229
[86] Horio Y, Hashimoto Y, Shiba K and Ichimiya A 1995 *Japan. J. Appl. Phys.* **34** 5869
[87] Horio Y and Hara T 2002 *Japan. J. Appl. Phys.* **41** L736
[88] Nakahara H, Hishida T and Ichimiya A 2003 *Appl. Suf. Sci.* **212–3** 157
[89] Tanishiro Y 2003 Hyomen Kagaku *J. Surf. Sci. Soc. Japan* **24** 166
[90] Inaoka T 1989 *Surf. Sci.* **208** 71
[91] Coleman P 2000 *Positron Beams and Their Applications* (London: World Scientific)
[92] Kawasuso A, Okada S and Ichimiya A 1999 *Nucl. Instrum. Methods Phys. Res.* B **171** 219
[93] Canter K F, Lippel P H, Crane W S and Mills A P Jr 1986 *Positron Studies of Solids, Surfaces, and Atoms* eds A P Mills Jr *et al* (Singapore: World Scientific) p 199
[94] Kawasuso A, Ishimoto T, Maekawa M, Fukaya Y, Hayashi K and Ichimiya A 2004 *Rev. Sci. Instrum.* **75** 4585
[95] Mills A P Jr 1980 *Appl. Phys.* **23** 189
[96] Mills A P Jr and Wilson R J 1982 *Phys. Rev.* A **26** 490
[97] Chen S M, Lynn K G, Pareja R and Nielsen B 1985 *Phys. Rev.* B **31** 4123
[98] Zafar N, Chevallier J, Laricchia G and Charlton M 1989 *J. Phys. D: Appl. Phys.* **22** 868
[99] Comsa G 1979 *Surf. Sci.* **81** 57
[100] Ichimiya A 1987 *Surf. Sci.* **192** L893